

Graduation Thesis 2017

Analysis of Measurement-based Quantum Network Coding over Repeater Networks under Noisy Conditions

量子中継器ネットワークのための測定型量子ネットワークコーディング プロトコルの提案およびノイズ下における性能評価

Keio University, Faculty of Environment and Information Studies
Takaaki Matsuo

Abstract of Bachelor's Thesis

Academic Year 2017

Analysis of Measurement-based Quantum Network Coding for Repeater Networks under Noisy Conditions

Similar to classical network coding, quantum network coding is an important technique for alleviating bottlenecks in quantum networks. This thesis considers a newly developed protocol, measurement-based quantum network coding for repeater networks (MQNC), and studies its behavior using Monte-Carlo simulation under noisy conditions. By exploiting measurement-based quantum computing, operation on qubits proceeds in parallel. This thesis shows that such an approach offers advantages over other schemes in terms of the quantum circuit depth. The circuit depth of MQNC has been reduced by 52% compared to the quantum network coding protocol (QNC) introduced in 2012 by Satoh, et al.

Evaluation of the circuit has been done through a comparison of the simulation results with Buffer-Space Multiplexing using entanglement swapping (ES) and QNC. The output fidelity in this thesis depends on the initial Bell pair fidelity and the local operation fidelity.

For MQNC, the resulting entangled pairs' joint fidelity drops below 50% when the accuracy of local operations is under 99%, assuming that all initial Bell pairs across quantum repeaters have a fixed fidelity of 98%. Overall, MQNC showed substantially higher error tolerance compared to QNC and slightly better than ES, but with no relative advantage over both protocols with the artificial model of only initial resource errors.

Keywords :

- 1. Quantum communication, 2. Quantum computation, 3. Quantum network coding,
- 4. Quantum repeater networks, 5. Network coding

Keio University, Faculty of Environment and Information Studies

Takaaki Matsuo

量子中継器ネットワークのための測定型量子ネットワークコーディング プロトコルの提案およびノイズ下における性能評価

量子通信における量子ネットワークコーディングは、古典通信におけるネットワークコーディングと同様に、量子ネットワークのボトルネックを緩和するための重要な技術である。しかし、現段階の既存研究成果は、バッファ空間多重化方式のような代替的な対応策に対して大きな優位性を示しきれていない。そこで、本研究では、量子中継機ネットワーク上において測定型量子計算を応用した量子ネットワークコーディング (MQNC) を提案する。提案したプロトコルは、古典ネットワークコーディングを模した手法ではなく、測定型量子計算を用いることでトポロジ的に量子ネットワークコーディングを行うことで、手順の並列化を実現した。その為、回路モデルの非測定型量子ネットワークコーディング (QNC) と比較して、量子回路の深さを約 52% に縮小することに成功した。

本研究の優位性を検証するため、モンテカルロ・シミュレーションによって量子回路へのノイズを再現した環境上において、既存研究であるエンタングルメント・スワッピングを使用したバッファ空間多重化方式 (ES)、および、QNC と統計的に比較することで性能評価実験を行った。シミュレーションの結果から、MQNC において量子通信リソースとしての Fidelity の最低値とされている $F_{output} = 50\%$ を保持するためには、初期値リソースの Fidelity が $F_{input} = 98\%$ の時、各ゲート操作の精度として最低でも $F_{operation} = 99\%$ が必要であることが立証された。また、MQNC は ES、QNC と比較して初期リソースエラーに対する耐性が低いものの、ゲートエラーや測定エラー等を含めた総合的なエラーに対する耐性は QNC の約 2 倍向上され、ES と比較しても優位であることが明らかとなった。

キーワード

1. 量子通信, 2. 量子計算, 3. 量子ネットワークコーディング, 4. 量子中継器ネットワーク,
5. ネットワークコーディング

慶應義塾大学 環境情報学部

松尾 賢明

Contents

1	Introduction	1
1.1	Background	1
1.2	Research Contribution	1
1.3	Thesis structure	2
2	Theory of Quantum Information	3
2.1	Historical background of Quantum Computation	3
2.2	Qubit	4
2.2.1	Dirac notation	4
2.2.2	Bloch sphere	5
2.2.3	Eigenvalue and Eigenvector	6
2.2.4	Measuring a qubit	6
2.3	Composite quantum systems	7
2.4	Entanglement	8
2.4.1	Bell pair/Einstein-Podolsky-Rosen (EPR) pair	8
2.4.2	W state	9
2.4.3	Greenberger-Horne-Zeilinger (GHZ) state	9
2.5	Density matrix	10
2.6	Fidelity	10
2.7	Quantum Gates	11
2.7.1	Single Qubit Gates	11
2.7.2	Measurement in a circuit	14
2.7.3	Controlled Gates	14
2.8	Cluster state/Graph state	15
2.9	Quantum Teleportation	16
2.10	Entanglement Swapping	18
2.11	Entanglement Purification	19
2.12	Error	20
2.13	Stabilizer	22
2.14	Quantum Repeater Network	22
2.15	Measurement-based Quantum Computation (MBQC)	23
3	Current State of Experimental Work	27
3.1	Satellite-based entanglement distribution over 1200 kilometers	27
3.2	Photon pair experiment and the violation of CHSH inequality	28

3.3	Experimental generation of cluster states	28
4	Related Work	30
4.1	Classical Network Coding	30
4.2	Multiplexing using Entanglement Swapping	31
4.2.1	Buffer-Space Multiplexing	31
4.2.2	Time-Division Multiplexing	32
4.3	Quantum Network Coding	33
4.3.1	Quantum Network Coding for Repeater networks	34
4.3.2	MBQC	37
5	Protocol Design	38
5.1	MQNC Protocol	38
5.1.1	1st Step: Initialization of Shared Resources	39
5.1.2	2nd Step: Creating 6-qubit cluster state	40
5.1.3	3rd Step: Creating 2 crossing-over cluster states	43
5.1.4	Compressing Quantum Circuit of MQNC	44
6	Evaluation	46
6.1	Environment	46
6.2	Common simulation settings	47
6.3	Simulation results and evaluation	48
6.3.1	Initial resource generation	48
6.3.2	Linear 3-qubit entanglement generation	52
6.3.3	Full MQNC circuit	55
7	Conclusion	66
	Acknowledgements	67

List of Figures

2.1	Quantum State described on a Bloch Sphere	6
2.2	Basic flow of quantum gate operation	11
2.3	Circuit representation of a Pauli-X gate	11
2.4	Circuit representation of a Pauli-Y gate	12
2.5	Circuit representation of a Pauli-Z gate	12
2.6	Circuit representation of an Hadamard gate	12
2.7	Circuit representation of a S gate	13
2.8	Circuit representation of a T gate	13
2.9	Circuit representation of a Measurement gate and its byproduct operator	14
2.10	Circuit representation of a Controlled-NOT gate	15
2.11	Circuit representation of a Controlled-Z gate	15
2.12	Simple quantum circuit of quantum teleportation	16
2.13	Simple quantum circuit of quantum teleportation without byproduct operations	17
2.14	Visualized model of quantum teleportation	17
2.15	Simple quantum circuit of entanglement swapping	18
2.16	Visualized model of entanglement swapping	19
2.17	Visualized model of entanglement purification	19
2.18	Error propagation of Hadamard gate	21
2.19	Error propagation of Controlled-Not gate	21
2.20	Error propagation of Controlled-Z gate	21
2.21	Error propagation of measurement	21
2.22	Architecture of a simple quantum repeater network	23
2.23	2D resource state generation	23
2.24	Quantum circuit for one-bit teleportation	23
2.25	One-bit teleportation to Measurement-based Quantum Computing	24
2.26	Measurement-based single qubit unitary operation	25
2.27	Measurement-based CNOT operation	25
2.28	Topological transition by measurements on 1D cluster states	25
2.29	Topological transition by measurements on 2D cluster states	26
3.1	Chinese satellite beaming down entangled photons to earth	27
4.1	Resource contention over Butterfly network	30
4.2	Network coding on a butterfly network	31
4.3	Simplified model of buffer-space multiplexing using entanglement swapping. The resource in the center link must be used shared.	32

4.4	Simplified model of time-division multiplexing using entanglement swapping. The center link must be used twice.	33
4.5	Step-by-step encoding procedure of QNC	36
4.6	Quantum circuit of QNC	36
4.7	Visualized encoding procedure of network coding on cluster state	37
5.1	Flow of MQNC encoding	39
5.2	2-qubit cluster state generation (a) Quantum circuit of 2-qubit cluster state generation (b) Simplified model of 2-qubit cluseter state generation	39
5.3	Stabilizer flow of 2-qubit cluster state generation circuit	40
5.4	3-qubit linear cluster state generation (a) Quantum circuit of linear 3-qubit cluster state generation (b) Simplified model of linear 3-qubit cluseter state generation	41
5.5	Y measurement performed on linear cluster state. (a) Quantum circuit of linear 3-qubit cluster state generation using Y measurement. (b) Simplified model of linear 3-qubit ccluseter state generation using Y measurement.	42
5.6	4-qubit star-shaped cluster state (a) Quantum circuit of 4-qubit star-shaped cluster state generation (b) Simplified model of linear 4-qubit star-shaped cluseter state generation	42
5.7	MQNC step2	42
5.8	MQNC step2 circuit	43
5.9	Simple circuit of MQNC	44
5.10	Compressed circuit of MQNC	45
5.11	Representation of compressed MQNC encoding	45
6.1	Quantum circuit for generating initial resources (a) Quantum circuit for Bell pair generation (b) Quantum circuit for 2 qubit cluster state generation	49
6.2	Impact of input fidelity to output fidelity in initial shared resource generation	50
6.3	Impact of local operation accuracy to output fidelity in initial shared resource generation. Input fidelity is fixed to $F_{input} = 0.98\%$	52
6.4	Quantum circuit for generating linear 3-qubit entanglement (a) Quantum circuit for GHZ state generation (b) Quantum circuit for 3 qubit cluster state generation.	52
6.5	Impact of input fidelity on output fidelity in linear 3-qubit entanglement generation	54
6.6	Impact of local gate accuracy on output fidelity in linear 3-qubit entanglement generation. Input fidelity is fixed to $F_{input} = 0.98\%$	55
6.7	Evaluated quantum circuits	56
6.8	Impact of input fidelity on output fidelity in three protocols. Probabilistic Z error on qubits labeled with odd numbers.	57
6.9	Impact of input fidelity on output fidelity in three protocols. Probabilistic X error on qubits labeled with odd numbers.	58

6.10 Impact of input fidelity on output fidelity in three protocols. Probabilistic errors on all qubits.	59
6.11 Impact of local operation accuracy to output fidelity in three protocols. Input fidelity is fixed to $F_{input} = 98\%$	60
6.12 Error distribution of one entangled outputs	62
6.13 Error distribution versus local operation accuracy in MQNC. Input fidelity is fixed to $F_{input} = 98\%$	64
6.14 Impact of local operation accuracy to output fidelity in three protocols. Memory error rate is fixed to $F_{memory} = 100\%$. Input fidelity is fixed to $F_{input} = 98\%$	65

List of Tables

2.1	Byproduct operations to complete quantum teleportation	17
2.2	Byproduct operations to complete entanglement swapping	19
2.3	Entanglement swapping with noisy Bell pairs	20
2.4	Different entangled states and the corresponding stabilizer sets	22
2.5	Byproduct operation to complete one-bit teleportation	24
5.1	Stabilizers after the Y measurement	41
5.2	Stabilizers of a butterfly cluster state : pre-measurement	43
5.3	Stabilizers of 2 crossing-over cluster states : post-measurement	44
6.1	Development environment	46
6.2	Simulation environment	47
6.3	Bell pair circuit error propagation of input error and the correlated output state. $ \psi_{init}\rangle = 0_20_1\rangle$ and $ \psi_{out}\rangle = \frac{1}{\sqrt{2}}(00\rangle + 11\rangle)$	49
6.4	Cluster state circuit error propagation of input error and the correlated output state. $ \psi_{init}\rangle = 0_20_1\rangle$ and $ \psi_{out}\rangle = \frac{1}{2}(00\rangle + 01\rangle + 10\rangle - 11\rangle)$	50
6.5	Possible types of errors caused by gate operations. (a) Error model of single-qubit gates where $ \psi_0\rangle$ is a quantum state and p = gate error rate. (b) Error model of two-qubit gates where $ \psi_{0,1}\rangle$ is a composite quantum state and p = gate error rate.	51
6.6	Possible types of errors on initial resources. (a) Error model of Bell pairs where $ \psi_{0,1}\rangle$ is a Bell pair and p = initial resource error rate. (b) Error model of cluster states where $ \psi_{0,1}\rangle$ is a cluster state and p = initial resource error rate.	53
6.7	Characteristics of Protocols	57
6.8	Characteristics of Protocols	61
6.9	Percentage difference of error distributions in MQNC	63
6.10	Percentage difference of error distributions in ES	63
6.11	Percentage difference of error distributions in QNC	63
6.12	Slope change of error rate by type. This reflects the sensitivity to each type of error.	64
6.13	Characteristics of Protocols with perfect memory	65

Chapter 1

Introduction

This chapter discusses the background, contribution of this thesis and the structure of the remaining chapters.

1.1 Background

Network coding, proposed by Ahlswede, Cai, Li, and Yeung [1], is a technique used for alleviating bottlenecks in a network, and therefore is capable of enhancing throughput for certain traffic patterns, by linearly combining messages and sending them simultaneously instead of just forwarding one by one. The linear combination of packets also contributes to the network robustness, mitigating packet losses and link failures without a need to re-transmit the original data from the source [2, 3].

Resource contention is not only a problem that occurs in classical networking but also in quantum. To tackle such issue, a number of quantum network coding techniques have been proposed. Unlike classical network coding, unknown quantum states cannot be replicated, which forbids the direct application of the classical approach to quantum network coding. While there are multiple protocols proposed that directly encode on the message qubits, the ability to manipulate the quantum channels also allows us to complete the quantum network coding without touching the message qubit until the very end of the protocol.

Recently introduced quantum network coding protocols are generally designed based on the classical algorithm, CNOT operation which is the quantum equivalent of XOR, and have high circuit complexities compared to general quantum routing protocol using entanglement swapping. As a consequence, prior work have not been able to demonstrate much advantage in terms of fidelity over simpler protocols such as the buffer-space multiplexing and the time-division multiplexing.

1.2 Research Contribution

The protocol that has been developed (MQNC) in this thesis does not imitate the classical network coding protocol (no use of CNOT operation which is the quantum equivalent of classical XOR) but instead introduces a completely different approach

by dynamically manipulating the network links using Measurement-based Quantum Computing (MBQC) and topologically completing the network coding. As a result, the circuit depth of MBQC has been halved compared to the quantum network coding protocol introduced in 2012 by Satoh et al [4].

Through the study of the designed protocol using Monte-Carlo simulation, the advantage of MQBC in terms of error tolerance over alternative solutions has been shown numerically. The simulation also revealed that having two byproduct operators for each measurement is not always a disadvantage but the synchronization of error propagations and cancellations can improve the joint fidelity of the two output entangled states. Lastly, this thesis clarified that qubit memories are the main causes of communication infidelity, and therefore should be improved prior to gate and measurement accuracies.

1.3 Thesis structure

The remaining of the thesis is constructed as follows. In Chapter 2, basics of quantum information are provided as a preliminary to support the readers with minimal knowledge. In Chapter 3, current status of experimental work is introduced. In Chapter 4, several related publications are briefly explained. In Chapter 5, the protocol design of measurement-based quantum network coding over repeater networks is being explained step-by-step in detail. In Chapter 6, main results of Monte-Carlo simulations are discussed with various settings over multiple protocols. Finally in Chapter 7, this thesis is concluded with some discussions regarding the future work.

Chapter 2

Theory of Quantum Information

2.1 Historical background of Quantum Computation

In 1982, a physicist named Richard Feynman [5], noted that it is generally not feasible to represent the results of quantum mechanics with a classical universal device. The newly introduced concept, quantum simulation, took the advantage of the puzzling quantum effects to effectively simulate physics, which can not be handled by ordinary computers regardless to its computation power.

The term "Quantum Computer" was officially used in print for the first time in 1985, by physicist David Deutsch [6]. He proposed a mathematical concept of a strictly modeled universal computer based on quantum mechanics with many properties not reproducible by classical Turing machines, and generalized computing methods for quantum computers.

Meanwhile, quantum networking appeared as a subfield of quantum computing. The algorithm named BB84, Quantum key distribution (QKD), was firstly proposed by Bennett and Brassard [7] in 1984, and came into the experimental forefront in 1989 [8]. The algorithm was widely recognized across the globe, as a result of its promising security by exploiting quantum mechanics.

Later on, in 1994, Peter Williston Shor [9] at Bell Laboratories introduced a quantum algorithm that has the capability of factorizing large numbers within polynomial time - known as Shor's algorithm. The algorithm essentially showed that quantum computers have abilities of breaking commonly used classical cryptography techniques based on prime number factorization such as the RSA cryptography.

The theoretical proposal of quantum teleportation, which is a technique to map an arbitrary state of qubit to another, was introduced by Bennett, Brassard, Crépeau et al [10]. A while after, it was successfully demonstrated experimentally and became one of the essential ingredients for quantum networking [11][12]. In order to achieve long distance quantum communication, intermediate nodes called "quantum repeaters" were introduced by Briegel and Dür [13] [14] in the late 1990s, as a tool for managing errors, creating entanglements and enabling multi-hop communications. Nevertheless, establishing a stable quantum communication over long distances still remains an outstanding challenge due to technical problems such as the operation errors and qubit

degradation.

2.2 Qubit

The indivisible unit of a classical information is known as *binary digit* or *bit*. A single bit has a single binary value that is not limited to, but in general expressed with 0 and 1. The two values of a bit in a classical computer may be represented by the electric charge stored in a capacitor, the direction of a magnetic field, or anything else that is capable of physically representing two values. Similarly, the smallest unit of a quantum information is known as *quantum bit* or *qubit*¹. Unlike a bit, a single qubit can be in a *superposition state* of two states, simultaneously representing 0 and 1. The two-level system of a quantum computer may be represented by the vertical polarization and the horizontal polarization of a photon, the spin up and the spin down of an electron, or any other proposed state variables.

2.2.1 Dirac notation

The simplest quantum system is a two-state system, and the single qubit pure state can be expressed by using the *Dirac notation*:

$$|\psi\rangle = \alpha|0\rangle + \beta|1\rangle$$

$$|\alpha|^2 + |\beta|^2 = 1 \quad (2.1)$$

Coefficients α and β are arbitrary complex numbers representing the probability amplitudes. The $|0\rangle$ and $|1\rangle$ are called *kets* and denote the two possible states, where the probability of the state being $|0\rangle$ can be found by the quantity $\alpha \times \alpha^* = |\alpha|^2$, and $\beta \times \beta^* = |\beta|^2$ for $|1\rangle$. As an example, $|\psi\rangle = \frac{1}{\sqrt{2}}|0\rangle + \frac{1}{\sqrt{2}}|1\rangle$ indicates that the state $|\psi\rangle$ is in a superposition of two states $|0\rangle$ and $|1\rangle$ with equally weighted probabilities.

A quantum state can also be described by a vector in a two dimensional complex Hilbert space. State vectors of a single qubit may be:

Z-basis state

$$|0\rangle \equiv \begin{bmatrix} 1 \\ 0 \end{bmatrix} \quad |1\rangle \equiv \begin{bmatrix} 0 \\ 1 \end{bmatrix} \quad (2.2)$$

Therefore, the superposition state of a single qubit can be expressed by the following two-dimensional vector.

$$|\psi\rangle = \alpha|0\rangle + \beta|1\rangle = \alpha \begin{bmatrix} 1 \\ 0 \end{bmatrix} + \beta \begin{bmatrix} 0 \\ 1 \end{bmatrix} = \begin{bmatrix} \alpha \\ \beta \end{bmatrix} \quad (2.3)$$

¹The term qubit just had its 25th anniversary.

The computational vectors introduced in equation 2.2 are called the Z-basis states, and a linear combination of them can be used to express any pure quantum state. The alternative computational bases, the *X-basis states* and the *Y-basis states* are equally important. The X-basis states are based on the superposition states:

(2.4)

X-basis state

$$|+\rangle \equiv \frac{1}{\sqrt{2}} \begin{bmatrix} 1 \\ 1 \end{bmatrix} \quad |-\rangle \equiv \frac{1}{\sqrt{2}} \begin{bmatrix} 1 \\ -1 \end{bmatrix}. \quad (2.5)$$

Similarly, the Y-basis states uses the complex bases:

(2.6)

Y-basis state

$$|+i\rangle \equiv \frac{1}{\sqrt{2}} \begin{bmatrix} 1 \\ i \end{bmatrix} \quad |-i\rangle \equiv \frac{1}{\sqrt{2}} \begin{bmatrix} 1 \\ -i \end{bmatrix}. \quad (2.7)$$

Contrasting to *ket*, $\langle \psi |$ is called *bra* which represents the conjugate transpose of $|\psi\rangle$.

$$|\alpha\rangle = \begin{bmatrix} \alpha_1 \\ \alpha_2 \\ \alpha_3 \\ \vdots \\ \alpha_n \end{bmatrix} \quad \langle \alpha | = [\alpha_1^* \ \alpha_2^* \ \alpha_3^* \ \cdots \ \alpha_n^*] \quad (2.8)$$

2.2.2 Bloch sphere

The Bloch sphere is a geometric representation of a single qubit pure state as a unit vector pointing on the surface of a unit sphere.

The arbitrary single qubit state can be written:

$$|\psi\rangle = e^{i\lambda} \left(\cos \frac{\theta}{2} |0\rangle + e^{i\phi} \sin \frac{\theta}{2} |1\rangle \right) \quad (2.9)$$

$$0 \leq \theta \leq \pi$$

$$0 \leq \phi \leq 2\pi$$

where variables θ , ϕ and λ are real numbers. The number θ represents the latitude with respect to Z-axis and ϕ represents the longitude with respect to Y-axis. Together they define a point on the Bloch sphere surface. The variable $e^{i\lambda}$ is known as the global phase of a quantum state, and has no observable effects. Therefore, equation 2.9 can simply be rewritten as:

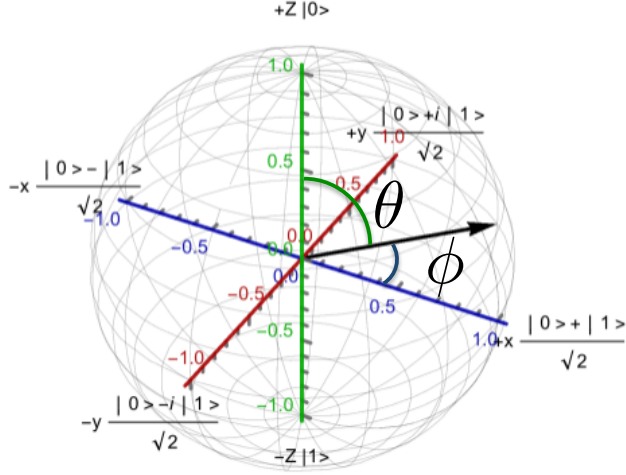


Figure 2.1: Quantum State described on a Bloch Sphere

$$|\psi\rangle = \cos \frac{\theta}{2} |0\rangle + e^{i\phi} \sin \frac{\theta}{2} |1\rangle \quad (2.10)$$

Hence, $\cos \frac{\theta}{2}$ and $e^{i\phi} \sin \frac{\theta}{2}$ correspond to α and β in equation 2.1 with α constrained to be real.

2.2.3 Eigenvalue and Eigenvector

The *eigenvalue* and the *eigenvector* are some important concepts for quantum information.

As an example, if an operator U acts on a vector $|\psi\rangle$ and the result can be rearranged to a scalar λ and the same vector $|\psi\rangle$:

$$U |\psi\rangle = \lambda |\psi\rangle \quad (2.11)$$

Such λ is called the *eigenvalue* and the corresponding vector $|\psi\rangle$ is called the *eigenvector*. In general, the eigenvalue is a complex number but here we often see it as a real number, ± 1 . For example, performing a Pauli-Z gate to a state $|1\rangle$ will result in:

$$Z |1\rangle = -|1\rangle \quad (2.12)$$

where in this case, the eigenvector of Z is $|1\rangle$ with an eigenvalue is -1.

2.2.4 Measuring a qubit

Measuring a qubit will destroy the superposition state and determine the state in a classical fashion. The measurement outcome of a quantum state is the eigenvalue of the eigenvector.

As an example, if the qubit state is:

$$|\psi\rangle = \frac{1}{\sqrt{2}}|0\rangle + \frac{1}{\sqrt{2}}|1\rangle = \begin{bmatrix} \frac{1}{\sqrt{2}} \\ \frac{1}{\sqrt{2}} \end{bmatrix} \quad (2.13)$$

the probability amplitude is equally weighted with respect to the Z-basis. Therefore, measuring the state in Z-basis will return the observer either $+Z$ or $-Z$ with a probability of 50%. Changing the measurement basis may affect the measurement result. That is to say, if we use the X-basis for the measurement instead of Z, then the measurement result will always be $+X$.

If we measure the qubit $|\psi\rangle$ in the Z-basis, measurement outcomes 0 and 1 can be obtained with probabilities:

$$P(0) = |\langle 0 | \psi \rangle|^2 = \text{Tr}[|0\rangle \langle 0 | \langle \psi | \psi \rangle] \quad (2.14)$$

$$P(1) = |\langle 1 | \psi \rangle|^2 = \text{Tr}[|1\rangle \langle 1 | \langle \psi | \psi \rangle] \quad (2.15)$$

More generally, the above equation can be expressed using measurement operators M_i .

$$P(i) = \langle \psi | M_i^\dagger M_i | \psi \rangle = \text{Tr}[M_i^\dagger M_i | \psi \rangle \langle \psi |] = \text{Tr}[E_i | \psi \rangle \langle \psi |] \quad (2.16)$$

where E_i is a set of positive operators such that $\sum_i E_i = I$.

The measurement operator can be obtained by:

$$M_i^\pm = \frac{1}{2}(I \pm U) \quad (2.17)$$

where U in this case is the matrix set $U = \{Z, Y, X\}$. As an example, the Z-basis measurement operators can be obtained by:

$$M_Z^+ = \frac{1}{2}(I + Z) = \frac{1}{2}\left(\begin{bmatrix} 1 & 0 \\ 0 & 1 \end{bmatrix} + \begin{bmatrix} 1 & 0 \\ 0 & -1 \end{bmatrix}\right) = \begin{bmatrix} 1 & 0 \\ 0 & 0 \end{bmatrix} \quad (2.18)$$

$$M_Z^- = \frac{1}{2}(I - Z) = \frac{1}{2}\left(\begin{bmatrix} 1 & 0 \\ 0 & 1 \end{bmatrix} - \begin{bmatrix} 1 & 0 \\ 0 & -1 \end{bmatrix}\right) = \begin{bmatrix} 0 & 0 \\ 0 & 1 \end{bmatrix} \quad (2.19)$$

2.3 Composite quantum systems

In reality, a system may contain more than one qubit. An independent two-qubit system may have states:

$$|\psi\rangle = \alpha|0\rangle + \beta|1\rangle \quad (2.20)$$

$$|\phi\rangle = \gamma|0\rangle + \delta|1\rangle \quad (2.21)$$

Here, the joint system can be described by taking the tensor product of equation 2.20 and equation 2.21.

$$|\psi\rangle \otimes |\phi\rangle = \alpha\gamma |00\rangle + \alpha\delta |01\rangle + \beta\gamma |10\rangle + \beta\delta |11\rangle = \begin{bmatrix} \alpha\gamma \\ \alpha\delta \\ \beta\gamma \\ \beta\delta \end{bmatrix} \quad (2.22)$$

$$|\alpha\gamma|^2 + |\alpha\delta|^2 + |\beta\gamma|^2 + |\beta\delta|^2 = 1$$

where \otimes is the tensor product of two vectors, and $|00\rangle$ equates to $|0\rangle|0\rangle$. The tensor product of two vectors is:

$$\begin{bmatrix} a_1 \\ b_1 \end{bmatrix} \otimes \begin{bmatrix} a_2 \\ b_2 \end{bmatrix} = \begin{bmatrix} a_1 \begin{bmatrix} a_2 \\ b_2 \end{bmatrix} \\ b_1 \begin{bmatrix} a_2 \\ b_2 \end{bmatrix} \end{bmatrix} = \begin{bmatrix} a_1 a_2 \\ a_1 b_2 \\ b_1 a_2 \\ b_1 b_2 \end{bmatrix} \quad (2.23)$$

The vector representation of two-qubit basis states are:

$$|00\rangle = \begin{bmatrix} 1 \\ 0 \\ 0 \\ 0 \end{bmatrix}, |01\rangle = \begin{bmatrix} 0 \\ 1 \\ 0 \\ 0 \end{bmatrix}, |10\rangle = \begin{bmatrix} 0 \\ 0 \\ 1 \\ 0 \end{bmatrix}, |11\rangle = \begin{bmatrix} 0 \\ 0 \\ 0 \\ 1 \end{bmatrix} \quad (2.24)$$

Similarly, three qubits can be in eight states, and n qubits can be in a superposition of all 2^n states simultaneously.

$$\sum_{i=0}^{2^n-1} \alpha_i |i\rangle \quad (2.25)$$

$$\sum_{i=0}^{2^n-1} |\alpha_i|^2 = 1$$

2.4 Entanglement

Two or more qubits can be in an *entangled* state, where each qubit's state cannot be described independently. That is to say, an operation on one entangled qubit will immediately affect the other pair regardless to the physical distance between.

2.4.1 Bell pair/Einstein-Podolsky-Rosen (EPR) pair

One common example of an entangled state is called *Bell pair* or sometimes called *EPR pair*:

$$|\psi\rangle = \frac{1}{\sqrt{2}}(|00\rangle + |11\rangle) = |\Phi^+\rangle \quad (2.26)$$

In the above example, note that each qubit state $|00\rangle$ and $|11\rangle$ have equally weighted probability, so that each qubit has a 50/50 probability of being found in each state but not independently. If one qubit's state is found to be 0, then the other qubit's state must be, and will be 0. Therefore, measuring one qubit will also decide the other qubit's state. Specifically, the four entangled states that can be used as a basis set is known as *Bell states*:

$$|\Phi^+\rangle = \frac{1}{\sqrt{2}}(|00\rangle + |11\rangle) \quad (2.27)$$

$$|\Phi^-\rangle = \frac{1}{\sqrt{2}}(|00\rangle - |11\rangle) \quad (2.28)$$

$$|\Psi^+\rangle = \frac{1}{\sqrt{2}}(|01\rangle + |10\rangle) \quad (2.29)$$

$$|\Psi^-\rangle = \frac{1}{\sqrt{2}}(|01\rangle - |10\rangle) \quad (2.30)$$

2.4.2 W state

The W state is an entangled quantum state that consists of 3 qubits, which has a similar state to the Φ^+ .

$$|W\rangle = \frac{1}{\sqrt{3}}(|001\rangle + |010\rangle + |100\rangle) \quad (2.31)$$

Measuring one qubit will result in either state:

$$|W^0\rangle = \frac{1}{\sqrt{2}}(|01\rangle + |10\rangle) \quad (2.32)$$

$$|W^1\rangle = |00\rangle \quad (2.33)$$

Depending on the measurement result, the residual system is entangled or unentangled.

2.4.3 Greenberger-Horne-Zeilinger (GHZ) state

The GHZ state is an entangled state of more than $N \geq 3$ qubits as in equation 2.34.

$$|\psi\rangle = \frac{1}{\sqrt{2}}(|0\rangle^{\otimes N} + |1\rangle^{\otimes N}) = |GHZ\rangle \quad (2.34)$$

The simplest GHZ state includes 3 qubits:

$$|\psi\rangle = \frac{1}{\sqrt{2}}(|0\rangle^{\otimes 3} + |1\rangle^{\otimes 3}) = \frac{1}{\sqrt{2}}(|000\rangle + |111\rangle) = |GHZ\rangle \quad (2.35)$$

Similar to a Bell pair, measuring an arbitrary qubit of the GHZ state decides the overall state to $|000\rangle$ or $|111\rangle$ with equally weighted probabilities. The GHZ state is not local operation and classical communication (LOCC) equivalent to the W state - no local operation can convert the GHZ state to the W state or vice versa.

2.5 Density matrix

Quantum states are either in mixed or pure state. A pure state is in a closed system, with no interaction with the outside world. In contrast, a mixed state is when a part of the quantum system becomes entangled with or is acted upon in unknown ways by the environment. While any pure state can be written in state-vector form, mixed states can be described using a *density matrix*. The density matrix of a pure state $|\psi\rangle$ can be found by:

$$\rho = |\psi\rangle\langle\psi| \quad (2.36)$$

The corresponding probability of a state $|j\rangle$ can be found by the diagonal entries of ρ :

$$P(|j\rangle) = \rho_{j,j} |j\rangle\langle j| \quad (2.37)$$

If the state is pure, $\rho^2 = \rho$ and $Tr[\rho^2] = 1$ and if the state is mixed $\rho^2 \neq \rho$ and $Tr[\rho^2] < 1$.

For example, the density matrix of a pure state Bell pair is:

$$\begin{aligned} \rho &= |\psi\rangle\langle\psi| = \frac{1}{\sqrt{2}}(|00\rangle + |11\rangle)\frac{1}{\sqrt{2}}(\langle 00| + \langle 11|) \\ &= \frac{1}{2}(|00\rangle\langle 00| + |00\rangle\langle 11| + |11\rangle\langle 00| + |11\rangle\langle 11|) = \begin{bmatrix} \frac{1}{2} & 0 & 0 & \frac{1}{2} \\ 0 & 0 & 0 & 0 \\ 0 & 0 & 0 & 0 \\ \frac{1}{2} & 0 & 0 & \frac{1}{2} \end{bmatrix} \end{aligned} \quad (2.38)$$

An example of a completely mixed state of 2 qubits, which represents the classical dependent probabilities is:

$$\rho = \frac{1}{2}(|00\rangle\langle 00| + |11\rangle\langle 11|) = \begin{bmatrix} \frac{1}{2} & 0 & 0 & 0 \\ 0 & 0 & 0 & 0 \\ 0 & 0 & 0 & 0 \\ 0 & 0 & 0 & \frac{1}{2} \end{bmatrix} \quad (2.39)$$

With a completely mixed state of 2 qubits, there is no entanglement between the two qubits - each has a state, $|0\rangle$ or $|1\rangle$.

The off-diagonal elements are quantum coherences and can be complex and the diagonal elements must be real.

2.6 Fidelity

The imperfection of a quantum state can be described by the *fidelity*. The fidelity is often defined as :

$$F = \sqrt{\langle\psi|\rho|\psi\rangle} \quad (2.40)$$

or more simply [15]:

$$F = \langle \psi | \rho | \psi \rangle \quad (2.41)$$

where $0 \leq F \leq 1$, $|\psi\rangle$ is the desired ideal state and ρ is the density matrix of the actual state. With $F = 1$, the actual state is identical to the desired state.

A single qubit system has a fidelity of 50% with a completely mixed state. Similarly, in n -qubit system, a completely mixed state has a fidelity of $F = \frac{1}{2^n}$.

2.7 Quantum Gates

As modern computers work based on logic gates, quantum computers performs similar gate operations to manipulate quantum information (see Figure 3.1 for a simplified model of gate operations). Such gates are often called unitary gates, as they give unitary transformation of the qubit states. Gates are unitary when $\dagger UU = U\dagger U = I$. Quantum gates are reversible and can be represented as unitary matrices.

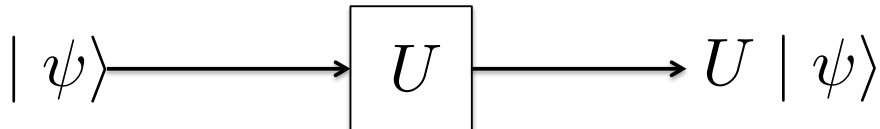


Figure 2.2: Basic flow of quantum gate operation

2.7.1 Single Qubit Gates

The most important operators for quantum computing are called the Pauli operators.

The Pauli-X gate is the equivalent of the classical NOT gate. The gate can be performed on a single qubit state and swaps the probability amplitude of $|0\rangle$ and $|1\rangle$.

$$X = \begin{bmatrix} 0 & 1 \\ 1 & 0 \end{bmatrix} \quad (2.42)$$

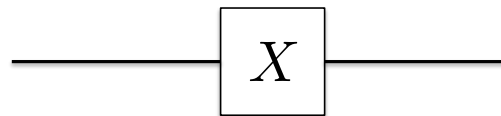


Figure 2.3: Circuit representation of a Pauli-X gate

Therefore, $|0\rangle = X|1\rangle$ and $|1\rangle = X|0\rangle$.

The Pauli-Y gate changes the quantum state $|0\rangle$ to $i|1\rangle$, and $|1\rangle$ to $-i|0\rangle$.

$$Y = \begin{bmatrix} 0 & -i \\ i & 0 \end{bmatrix} \quad (2.43)$$

The Pauli-Z gate, or sometimes called the phase-flip gate, does not affect the basis state $|0\rangle$, but changes $|1\rangle$ to $-|1\rangle$, and $-|1\rangle$ to $|1\rangle$.

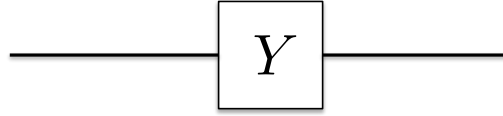


Figure 2.4: Circuit representation of a Pauli-Y gate

$$Z = \begin{bmatrix} 1 & 0 \\ 0 & -1 \end{bmatrix} \quad (2.44)$$

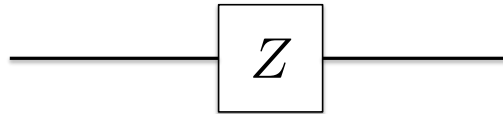


Figure 2.5: Circuit representation of a Pauli-Z gate

Besides Pauli operators, the Hadamard gate and the Phase gate are equally important operators. These gates can be used to transform between the different basis states.

The Hadamard gate is as shown below.

$$H = \frac{1}{\sqrt{2}} \begin{bmatrix} 1 & 1 \\ 1 & -1 \end{bmatrix} \quad (2.45)$$

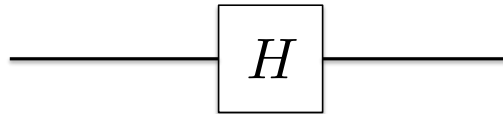


Figure 2.6: Circuit representation of an Hadamard gate

Applying an Hadamard gate to a qubit will result in:

$$H |0\rangle = \frac{1}{\sqrt{2}} \begin{bmatrix} 1 & 1 \\ 1 & -1 \end{bmatrix} \begin{bmatrix} 1 \\ 0 \end{bmatrix} = \frac{1}{\sqrt{2}} \begin{bmatrix} 1 \\ 1 \end{bmatrix} = |+\rangle \quad (2.46)$$

$$H |1\rangle = \frac{1}{\sqrt{2}} \begin{bmatrix} 1 & 1 \\ 1 & -1 \end{bmatrix} \begin{bmatrix} 0 \\ 1 \end{bmatrix} = \frac{1}{\sqrt{2}} \begin{bmatrix} 1 \\ -1 \end{bmatrix} = |-\rangle \quad (2.47)$$

$$H |+\rangle = \frac{1}{\sqrt{2}} \begin{bmatrix} 1 & 1 \\ 1 & -1 \end{bmatrix} \begin{bmatrix} 1 \\ 1 \end{bmatrix} = \frac{1}{\sqrt{2}} \begin{bmatrix} 1 \\ 0 \end{bmatrix} = |0\rangle \quad (2.48)$$

$$H |-\rangle = \frac{1}{\sqrt{2}} \begin{bmatrix} 1 & 1 \\ 1 & -1 \end{bmatrix} \begin{bmatrix} 1 \\ -1 \end{bmatrix} = \frac{1}{\sqrt{2}} \begin{bmatrix} 0 \\ 1 \end{bmatrix} = |1\rangle \quad (2.49)$$

Notice that an Hadamard gate can bring up a qubit into a superposition state from a basis state, or vice versa. Moreover, the X gate can be constructed by conjugating two Hadamard gates and a Z gate: $X = HZH$.

Similar to the Z gate, the phase shift gate changes the phase of a quantum state, from $|1\rangle$ to $e^{i\phi}|1\rangle$. Therefore, if $\phi = \pi$, the phase gate performs on a qubit the same way as the Z gate. T gate and S gate are for specific, defined values of ϕ .

$$Z_\phi = \begin{bmatrix} 1 & 0 \\ 0 & e^{i\phi} \end{bmatrix} \quad (2.50)$$

$$S = Z_{\frac{\pi}{2}} = \begin{bmatrix} 1 & 0 \\ 0 & e^{i\frac{\pi}{2}} \end{bmatrix} \quad (2.51)$$

$$T = Z_{\frac{\pi}{4}} = \begin{bmatrix} 1 & 0 \\ 0 & e^{i\frac{\pi}{4}} \end{bmatrix} \quad (2.52)$$

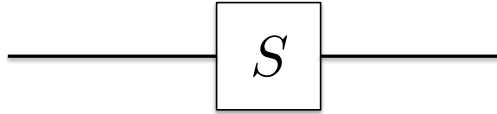


Figure 2.7: Circuit representation of a S gate

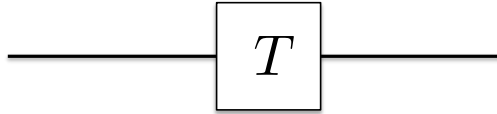


Figure 2.8: Circuit representation of a T gate

S gates and X gate can be used to construct Y gate: $Y = SXS^\dagger$. A gate that rotates the quantum state by 180 degrees does not get affected by the rotational direction; clockwise or anti-clockwise. As an S gate sometimes performs a rotation of less than 180 degrees, the direction of rotation matters. The clockwise rotation is represented with S gate, and the anti-clockwise rotation is represented by the dagger of the gate S^\dagger or sometimes S^- .

The rotation operator, which rotates the Bloch vector about the X, Y and Z-axis by a given angle θ , can be described as $R_P(\theta) = e^{-i\frac{\theta}{2}P}$, where P represents the axis.

$$R_X(\theta) = e^{-i\frac{\theta}{2}X} = \cos \frac{\theta}{2}I - i \sin \frac{\theta}{2}X = \begin{bmatrix} \cos \frac{\theta}{2} & -i \sin \frac{\theta}{2} \\ -i \sin \frac{\theta}{2} & \cos \frac{\theta}{2} \end{bmatrix} \quad (2.53)$$

$$R_Y(\theta) = e^{-i\frac{\theta}{2}Y} = \cos \frac{\theta}{2}I - i \sin \frac{\theta}{2}Y = \begin{bmatrix} \cos \frac{\theta}{2} & -\sin \frac{\theta}{2} \\ \sin \frac{\theta}{2} & \cos \frac{\theta}{2} \end{bmatrix} \quad (2.54)$$

$$R_Z(\theta) = e^{-i\frac{\theta}{2}Z} = \cos \frac{\theta}{2}I - i \sin \frac{\theta}{2}Z = \begin{bmatrix} e^{-i\frac{\theta}{2}} & 0 \\ 0 & e^{i\frac{\theta}{2}} \end{bmatrix} \quad (2.55)$$

$$(2.56)$$

2.7.2 Measurement in a circuit

The measurement result of an arbitrary qubit, if any, decides the residual quantum state. That is to say, two post-measurement residue states may not equate depending on the measurement results, even with two identical pre-measurement quantum systems. Therefore, in MBQC, measurement requires a classical feedforward operation to another qubit to fix the state to a wanted form - sometimes to more than one qubit. Those operators are often called *byproduct operators* and are performed based on classically sent measurement results. As shown in the circuit representation below at Figure 2.9, the classical message transmission is generally described with double lines interconnecting the measurement operator and the byproduct operator.

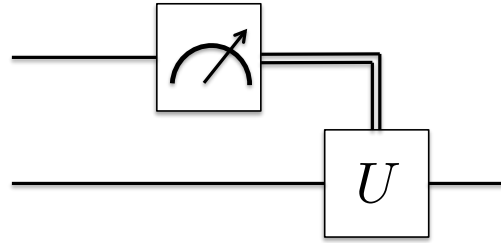


Figure 2.9: Circuit representation of a Measurement gate and its byproduct operator

2.7.3 Controlled Gates

Not all gates work on single qubit; some act on two or more qubits. One example of such gate is the Controlled-NOT (CNOT) gate that performs X gate on one qubit (*the target qubit*), if another qubit's (*the control qubit*) state is $|1\rangle$. The CNOT gate is defined by:

$$\Lambda_{c,t}(X) |i_c\rangle |j_t\rangle = |i_c\rangle |i \oplus j_t\rangle \quad (2.57)$$

$$i, j = 0, 1 \quad (2.58)$$

And the corresponding matrix is:

$$CNOT = \begin{bmatrix} 1 & 0 & 0 & 0 \\ 0 & 1 & 0 & 0 \\ 0 & 0 & 0 & 1 \\ 0 & 0 & 1 & 0 \end{bmatrix} \quad (2.59)$$

Similarly, the Controlled-Z (CZ) gate performs the Z operation on the target qubit, when the controlled qubit's state is $|1\rangle$. The CZ gate is defined by:

$$\Lambda_{c,t}(Z) |i_c\rangle |j_t\rangle = (-1)^{ij} |i_c\rangle |j_t\rangle \quad (2.60)$$

$$i, j = 0, 1 \quad (2.61)$$

The CZ gate is symmetric, $\Lambda_{c,t}(Z) = \Lambda_{t,c}(Z)$ and the corresponding matrix is:

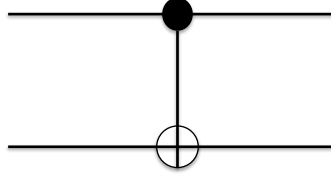


Figure 2.10: Circuit representation of a Controlled-NOT gate

$$CZ = \begin{bmatrix} 1 & 0 & 0 & 0 \\ 0 & 1 & 0 & 0 \\ 0 & 0 & 1 & 0 \\ 0 & 0 & 0 & -1 \end{bmatrix} \quad (2.62)$$

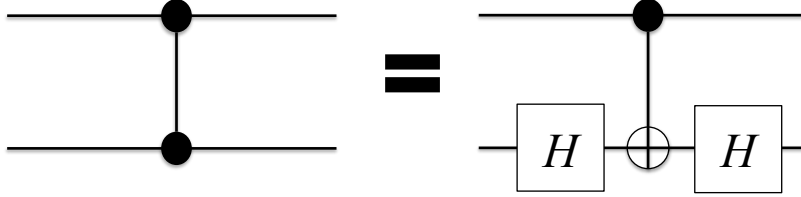


Figure 2.11: Circuit representation of a Controlled-Z gate

2.8 Cluster state/Graph state

A cluster state, or sometimes called graph state, is an example of qubits that are maximally entangled - a maximally entangled state has the maximum Von Neumann entropy obtainable by the number of qubits in the system. The Von Neumann entropy is a measure of entanglement:

$$S(\rho) = -\text{Tr } \rho \log_2(\rho) \quad (2.63)$$

A cluster state of n vertices (qubits) can be defined by:

$$|G\rangle = \prod_{(a,b) \in E} \Lambda_{a,b}(Z) |+\rangle^{\otimes n} \quad (2.64)$$

where E is the set of edges (entanglement) and a, b are the corresponding vertices (qubits).

As an example, 3-qubit cluster state is:

$$|\psi\rangle = \frac{1}{2\sqrt{2}}(|0_10_20_3\rangle + |0_10_21_3\rangle + |0_11_20_3\rangle - |0_11_21_3\rangle + |1_10_20_3\rangle + |1_10_21_3\rangle - |1_11_20_3\rangle + |1_11_21_3\rangle) \quad (2.65)$$

where the subscript denotes the labeled number for identification. All states are equally weighted, and measuring qubit 1 will result in either one of the following system:

If the measurement result is 0

$$|\psi^0\rangle = \frac{1}{2}(|0_20_3\rangle + |0_21_3\rangle + |1_20_3\rangle - |1_21_3\rangle) \quad (2.66)$$

If the measurement result is 1

$$|\psi^1\rangle = \frac{1}{2}(|0_20_3\rangle + |0_21_3\rangle - |1_20_3\rangle + |1_21_3\rangle) \quad (2.67)$$

The equation 2.67 equates to equation 2.66 with an additional Z operation to qubit 2 as a byproduct, $|\psi^0\rangle = Z_1|\psi^1\rangle$. Notice that measuring just one qubit does not fully decide the remaining state. The 2-qubit cluster state is also LOCC equivalent to the Bell pair.

2.9 Quantum Teleportation

Using gate operations, it is possible to teleport quantum information from one place to another. This is not only limited to close distance but also for long distances. The simplest circuit implementation for quantum teleportation is as shown in Figure 2.12.

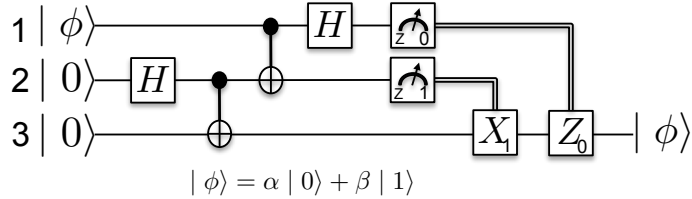


Figure 2.12: Simple quantum circuit of quantum teleportation

As shown in the above circuit, each measurement comes with a classical feedforward operation to the residual qubit, which is essential for completing the teleportation of an arbitrary quantum state. Even though entangled particles always share physical properties regardless of the distance between, the necessity of classical communication forbids the transmission of information from one place to another faster than the speed of light.

$$\begin{aligned}
H_1\Lambda_{1,2}(X)\Lambda_{2,3}(X)H_2|0_3\rangle|0_2\rangle|\Phi_1\rangle &= H_1\Lambda_{1,2}(X)\Lambda_{2,3}(X)H_2|0_30_2\rangle \otimes \alpha|0_1\rangle + \beta|1_1\rangle \\
&= H_1\Lambda_{1,2}(X)\left(\frac{1}{\sqrt{2}}(|0_30_2\rangle + |1_21_3\rangle)\right) \otimes \alpha|0_1\rangle + \beta|1_1\rangle \\
&= H_1\left(\frac{1}{\sqrt{2}}(\alpha|0_10_20_3\rangle + \alpha|1_11_21_3\rangle + \beta|1_10_20_3\rangle + \beta|1_11_21_3\rangle)\right) \\
&= \left(\frac{1}{2}(\alpha|0_10_20_3\rangle + \alpha|1_10_20_3\rangle + \alpha|0_11_21_3\rangle + \alpha|1_11_21_3\rangle \right. \\
&\quad \left. - \beta|1_11_20_3\rangle + \beta|0_11_20_3\rangle - \beta|1_10_21_3\rangle + \beta|0_10_21_3\rangle)\right)
\end{aligned} \quad (2.68)$$

Depending on the measurement results, byproduct operations are applied to the remaining qubit to complete the teleportation. For details, see Table 2.1. Each outcome can be found with equal probability of 25%.

Table 2.1: Byproduct operations to complete quantum teleportation

Measurement result	Output state	Byproduct operation
$0_1 0_2$	$\alpha 0_3\rangle + \beta 1_3\rangle$	I
$0_1 1_2$	$\alpha 1_3\rangle + \beta 0_3\rangle$	X
$1_1 0_2$	$\alpha 0_3\rangle - \beta 1_3\rangle$	Z
$1_1 1_2$	$\alpha 1_3\rangle - \beta 0_3\rangle$	XZ

Notice that when the measurement result of qubit 2 is 1, there is always a bit-flip error on the remaining qubit. Similarly, when the measurement result of qubit 1 is 1, Z gate is must be applied to qubit 3 as a byproduct to fix the phase. Thus, qubit 3's state can be manipulated beforehand to avoid any byproduct operation after the measurement as in Figure 2.13. The communication speed is still not faster than the speed of light as qubit 3, which is a part of the Bell pair, needs to be sent to another node to establish a long distance communication.

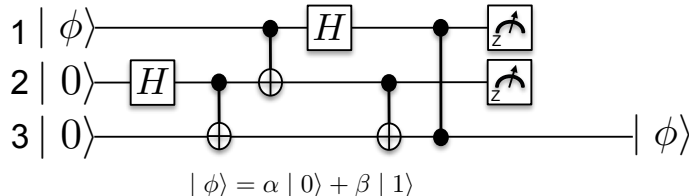


Figure 2.13: Simple quantum circuit of quantum teleportation without byproduct operations

The visualized model of quantum teleportation is shown in Figure 2.14.

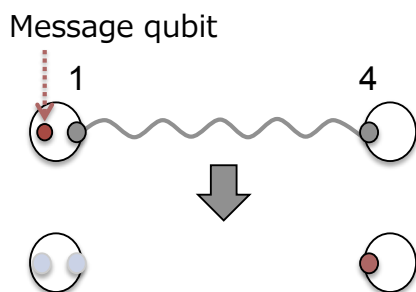


Figure 2.14: Visualized model of quantum teleportation

2.10 Entanglement Swapping

The quantum teleportation technique introduced above is an example of transmitting one bit of quantum information from one place to another but networking often requires multi-hop communication. The simplest solution for such demand is to apply quantum teleportation hop-by-hop. Nevertheless, operating on the message qubit directly many times degrades the information. Another solution is the use of *entanglement swapping* [16], which is capable of lengthening the Bell pair to allow a direct teleportation of quantum information over multiple repeaters. As shown in Figure 2.15, entanglement swapping is based on the teleportation circuit that was introduced above and in Figure 2.12. In the below example, 2 Bell pairs are consumed to output 1 end-to-end Bell pair.

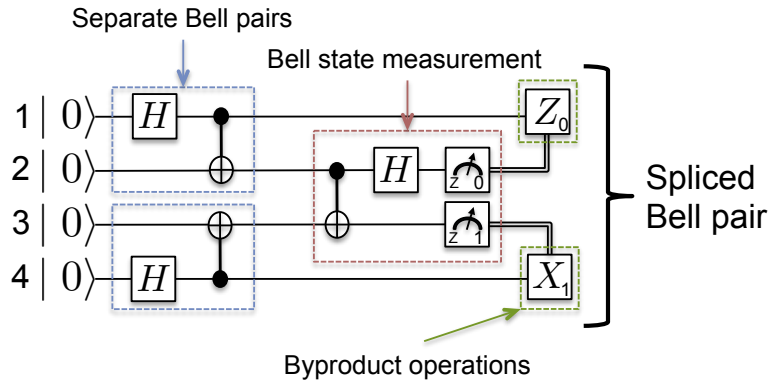


Figure 2.15: Simple quantum circuit of entanglement swapping

Subscripts of operators are identifiers for clarifying the interconnection between the measurement operator and its byproduct operator.

$$\begin{aligned}
 & H_2 \Lambda_{2,3}(X) \Lambda_{4,3}(X) \Lambda_{1,2}(X) H_4 H_1 |0_4\rangle |0_3\rangle |0_2\rangle |0_1\rangle \\
 &= H_2 \Lambda_{2,3}(X) \frac{1}{\sqrt{2}} (|0_1 0_2\rangle + |1_1 1_2\rangle) \otimes \frac{1}{\sqrt{2}} (|0_3 0_4\rangle + |1_3 1_4\rangle) \\
 &= H_2 \frac{1}{2} (|0_1 0_2 0_3 0_4\rangle + |0_1 0_2 1_3 1_4\rangle + |1_1 1_2 1_3 0_4\rangle + |1_1 1_2 0_3 1_4\rangle) \\
 &\quad \frac{1}{2\sqrt{2}} (|0_1 0_2 0_3 0_4\rangle + |0_1 1_2 0_3 0_4\rangle + |0_1 0_2 1_3 1_4\rangle + |0_1 1_2 1_3 1_4\rangle \\
 &\quad - |1_1 1_2 1_3 0_4\rangle + |1_1 0_2 1_3 0_4\rangle - |1_1 1_2 0_3 1_4\rangle + |1_1 0_2 0_3 1_4\rangle)
 \end{aligned} \tag{2.69}$$

Table 2.2: Byproduct operations to complete entanglement swapping

Measurement result	Output state	Byproduct operation
0_20_3	$\frac{1}{\sqrt{2}}(0_10_4\rangle + 1_11_4\rangle)$	I
0_21_3	$\frac{1}{\sqrt{2}}(0_11_4\rangle + 1_10_4\rangle)$	X_4
1_20_3	$\frac{1}{\sqrt{2}}(0_10_4\rangle - 1_11_4\rangle)$	Z_1
1_21_3	$\frac{1}{\sqrt{2}}(0_11_4\rangle - 1_10_4\rangle)$	X_4Z_1

The byproduct operator, Z gate, can also be applied to qubit 4 instead of qubit 1. The visualized model is at Figure 2.16.

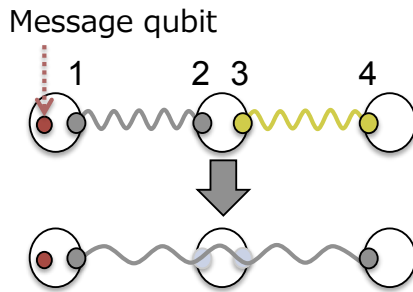


Figure 2.16: Visualized model of entanglement swapping

2.11 Entanglement Purification

Using two or more less-entangled mixed pairs shared among nodes, it is possible to create one pair with a higher entanglement. The easiest example of entanglement purification can be shown using 2 Bell pairs as in Figure 2.17.

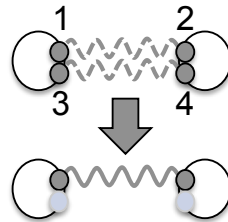


Figure 2.17: Visualized model of entanglement purification

In this example, two Bell pairs $|\Phi_{1,2}^+\rangle$, $|\Phi_{3,4}^+\rangle$ are shared between two nodes which are physically far apart, each holding half of the two pairs. In order to create and check the parity of two qubits in each node, both nodes locally perform a CNOT operation and measure one of the pairs with respect to the Z-basis, which destroys one Bell pair. If the measurement results agree, 0_30_4 or 1_31_4 , the remaining pair will have a higher fidelity than the original pairs given $F_{input} > 50\%$. On the other hand, the whole resource needs to be discarded if the measurement results do not agree.

When Bell pairs are both perfect and gates have no noise $F_{input} = 1.00$ and $F_{operation} = 1.00$:

$$\begin{aligned}
\Lambda_{2,4}(X)\Lambda_{1,3}(X) |\Phi_{1,2}^+\rangle |\Phi_{3,4}^+\rangle &= \Lambda_{2,4}(X)\Lambda_{1,3}(X) \frac{1}{\sqrt{2}}(|0_10_2\rangle) \otimes \frac{1}{\sqrt{2}}(|0_30_4\rangle) \\
&= \Lambda_{2,4}(X)\Lambda_{1,3}(X) \frac{1}{2}(|0_10_20_30_4\rangle + |0_10_21_31_4\rangle + |1_11_20_30_4\rangle + |1_11_21_31_4\rangle) \\
&= \Lambda_{2,4}(X) \frac{1}{2}(|0_10_20_30_4\rangle + |0_10_21_31_4\rangle + |1_11_21_30_4\rangle + |1_11_20_31_4\rangle) \\
&= \frac{1}{2}(|0_10_20_30_4\rangle + |0_10_21_31_4\rangle + |1_11_21_31_4\rangle + |1_11_20_30_4\rangle) \\
&= |\Phi_{1,2}^+\rangle |\Phi_{3,4}^+\rangle \quad (2.70)
\end{aligned}$$

When either Bell pair is imperfect, a bit-flip error on $|\Phi^+\rangle$ changes the state to $|\Psi^+\rangle$. Below is the summary of the behavior when $F_{output} > F_{input}$ and $F_{input} > 0.5$.

Table 2.3: Entanglement swapping with noisy Bell pairs

Input state	Probability	Output state	Result
$ \Phi_{1,2}^+\rangle \Phi_{3,4}^+\rangle$	F^2	$ \Phi_{1,2}^+\rangle$	True positive
$ \Phi_{1,2}^+\rangle \Psi_{3,4}^+\rangle$	$F(1 - F)$	-	True negative
$ \Psi_{1,2}^+\rangle \Phi_{3,4}^+\rangle$	$F(1 - F)$	-	False negative
$ \Psi_{1,2}^+\rangle \Psi_{3,4}^+\rangle$	$(1 - F)^2$	$ \Psi_{1,2}^+\rangle$	False positive

With an assumption of two Bell pairs having the same fidelity, the probability of getting the same measurement results can be obtained by $F_{input}^2 + (1 - F_{input})^2$, while the probability of it actually being right is F_{input}^2 . Therefore, The relation between the input fidelity and the output fidelity after performing entanglement purification can be derived as:

$$F_{output} = \frac{F_{input}^2}{F_{input}^2 + (1 - F_{input})^2} \quad (2.71)$$

The iteration of the above steps can be used to create an entangled pair of arbitrarily high purity $F_{out} < 1$.

2.12 Error

Quantum gates are inherently noisy, and may cause errors while operating on qubits. In general, there are two types of errors that should be taken into consideration, the bit-flip (X) error and the phase (Z) error - the Y error is a combination of both errors.

Equally important, errors may propagate through quantum circuits throughout the operation. The Hadamard gate converts bit-flip error to phase error, and phase error to bit-flip error.

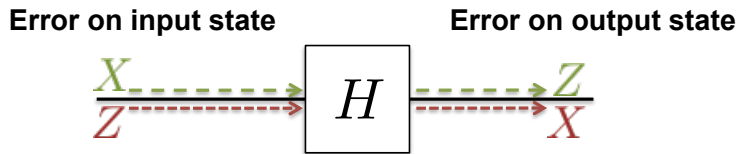


Figure 2.18: Error propagation of Hadamard gate

The CNOT operation will result in a propagation of the bit-flip error on the control qubit, ending up with bit-flip errors on both qubits. Similarly, a phase error on the target qubit will be transferred, after application of CNOT gate, to the control qubit.

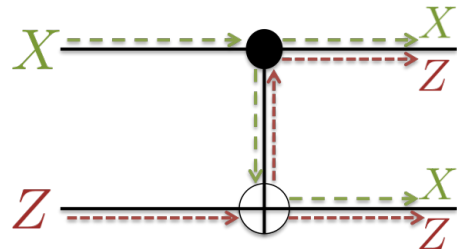


Figure 2.19: Error propagation of Controlled-Not gate

Similarly, the bit-flip error on the control qubit will result in a bit-flip error on the target qubit and a phase error on the control qubit after the CZ operation. Furthermore, a bit-flip error on the target qubit will result in a bit-flip error on the target qubit and a phase error on the control qubit.

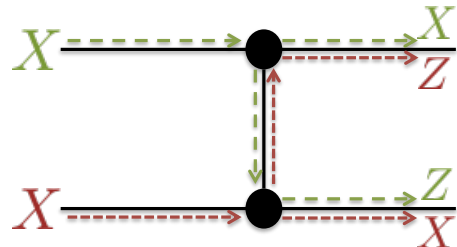


Figure 2.20: Error propagation of Controlled-Z gate

The measurement outcome depends on the quantum state, and thus a measurement error leads to a errory feedforward operation. Therefore measurement errors in MBQC also propagates to other qubits through byproduct operations.

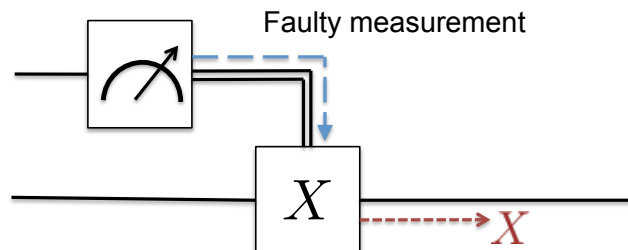


Figure 2.21: Error propagation of measurement

2.13 Stabilizer

A quantum state may be described by a state vector or a density matrix. An alternative way to represent a pure state is to use a set of stabilizers. A stabilizer S of a state $|\psi\rangle$ is:

$$S |\psi\rangle = |\psi\rangle \quad (2.72)$$

Consequently, a stabilizer or a set of stabilizers uniquely determines a quantum state. Below are examples of stabilizers for different states:

$$Z |0\rangle = |0\rangle \quad -Z |1\rangle = |1\rangle \quad (2.73)$$

$$X |+\rangle = |+\rangle \quad -X |-\rangle = |-\rangle \quad (2.74)$$

$$Y |+\rangle = |+i\rangle \quad -Y |-\rangle = |-i\rangle \quad (2.75)$$

Stabilizers for entangled states are:

Table 2.4: Different entangled states and the corresponding stabilizer sets

Quantum state	Stabilizer sets
$\frac{1}{\sqrt{2}}(0_10_2\rangle + 1_11_2\rangle)$	X_1X_2, Z_1Z_2
$\frac{1}{\sqrt{2}}(0_10_2\rangle - 1_11_2\rangle)$	$-X_1X_2, Z_1Z_2$
$\frac{1}{\sqrt{2}}(0_11_2\rangle + 1_10_2\rangle)$	$X_1X_2, -Z_1Z_2$
$\frac{1}{\sqrt{2}}(0_11_2\rangle - 1_10_2\rangle)$	$-X_1X_2, -Z_1Z_2$
$\frac{1}{\sqrt{2}}(0_10_20_3\rangle + 0_10_20_3\rangle)$	$X_1X_2X_3, Z_1Z_2, Z_2Z_3$
$\frac{1}{\sqrt{2}}(0_1+2\rangle - 1_1-2\rangle)$	X_1Z_2, Z_1X_2
$\frac{1}{2}(0_10_2+3\rangle + 0_11_2-3\rangle + 1_11_2+3\rangle 1_11_2-3\rangle +)$	$X_1Z_2, Z_1X_2Z_3, Z_2X_3$

So $|\psi\rangle$ is the eigenvector of all stabilizers inset. A quantum state with n qubits can be fully described by n stabilizers. Stabilizers can be helpful when describing a state consisting of many qubits, as the number of stabilizers grows only linearly while other methods grow exponentially. On the other hand, finding the correct stabilizer set that corresponds to a particular complex quantum state is difficult. Moreover, stabilizers can be only used to represent states manipulated with Clifford group operations.

2.14 Quantum Repeater Network

A quantum repeater network is a system consisting of quantum repeaters, which are composed of undirected classical channels, quantum channels and memory qubits, as shown below in Figure 2.22. The main role of a quantum repeater is to extend the communication range by managing errors, creating entanglement between neighboring nodes, enabling multi-hop communications.

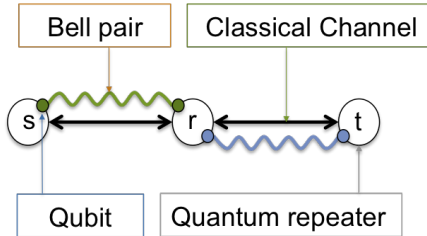


Figure 2.22: Architecture of a simple quantum repeater network

2.15 Measurement-based Quantum Computation (MBQC)

Measurement-based Quantum Computation (MBQC) is an alternative universal computation method based on single qubit measurements that was proposed by Raussendorf, Browne and Briegel in 2003 [17] - also known as one-way quantum computing. Unlike the circuit model, the scheme of MBQC generally requires a two dimensional grid of qubits that are initialized as $|+\rangle$ and entangled with all neighboring qubits using CZ gates, as a cluster state (see Figure 2.23). The initialized cluster state for MBQC is also called the *resource state*.

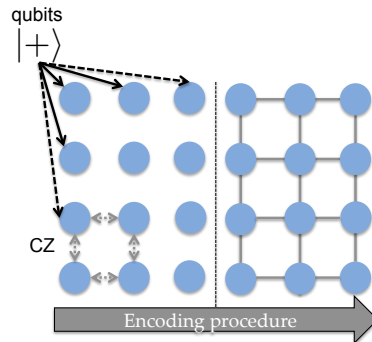


Figure 2.23: 2D resource state generation

The technique to map an unknown quantum state from one qubit to another is known as *one-bit teleportation* (see Figure 2.24) - introduced by Zhou, Leung and Chuang in 2000 [18].

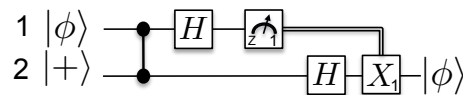


Figure 2.24: Quantum circuit for one-bit teleportation

The calculation using state-vector form is:

$$\begin{aligned}
H_1 \Lambda_{1,2}(Z) |\phi_1\rangle |+_2\rangle &= H_1 \Lambda_{1,2}(Z) \alpha |0\rangle + \beta |1\rangle \otimes |+_2\rangle \\
&= H_1 \alpha |0_1 +_2\rangle + \beta |1_1 -_2\rangle \\
&= \alpha |+_1 +_2\rangle + \beta |-_1 -_2\rangle
\end{aligned} \tag{2.76}$$

After the measurement operations, the residual state ends up in either output state in Table 2.5.

Table 2.5: Byproduct operation to complete one-bit teleportation

Measurement result	Output state	Byproduct operation
0_1	$\alpha +\rangle + \beta -\rangle$	$(H_2)I$
1_1	$\alpha +\rangle - \beta -\rangle$	$(H_2)X_2$

The X gate in this case behaves like a Z gate on $|0\rangle, |1\rangle$ basis. The Hadamard gate is used to convert the state $|+\rangle$ to $|0\rangle$ and $|-\rangle$ to $|1\rangle$.

Inserting a $R_Z(\theta)$ operation to the one-bit teleportation circuit can simply be accomplished by adding the gate just before the CZ gate (shown Figure 2.25(a)). As $R_Z(\theta)|\phi\rangle$ can be considered as state $|\phi'\rangle$, the circuit can be directly related to the circuit in Figure 2.24. However, as rotations across Z-axis commute with the CZ operation, the circuit can be rewritten as Figure 2.25(b). The set of operations on qubit 1 after the CZ gate can be considered as a single measurement operator in a particular basis, and the overall protocol can be simplified to a collection of CZ gates and measurement operations. Finally, the computation depends on the measurement basis, which specifies the θ .

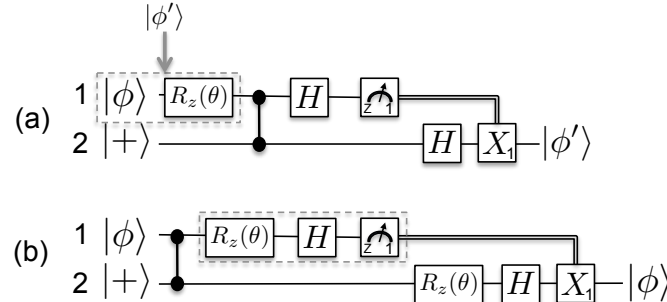


Figure 2.25: One-bit teleportation to Measurement-based Quantum Computing

An arbitrary single qubit unitary operation U can be decomposed into Euler angles:

$$U = He^{i\theta Z} e^{i\phi X} e^{i\xi Z} = He^{i\theta Z} He^{i\phi Z} He^{i\xi Z} \tag{2.77}$$

as an X gate can also be described by two Hadamard gates and a Z gate $X = HZH$. Therefore, an arbitrary single qubit unitary operation can be represented by a sequence of one-bit teleportations.

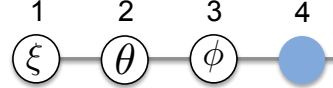


Figure 2.26: Measurement-based single qubit unitary operation

The realization of the CNOT operation can be accomplished by a 2-dimensional sequence of measurements as shown in Figure 2.27 below. Z-basis measurements are performed beforehand to omit unwanted qubits from the graph.

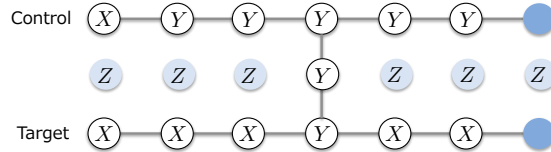


Figure 2.27: Measurement-based CNOT operation

Performing Pauli basis measurements transforms the graph states. Considering a 1D cluster state, the Z-basis measurement removes the measured qubit and disconnects the links, leaving two separate cluster states, or two independent qubits with a state $|1\rangle$ respectively (see Figure 2.28(a)). The Y-basis measurement also removes the measured qubit but directly connects the neighbors up to the phase operations as a byproduct (see Figure 2.28(b)). Unlike the other Pauli basis measurements, the X-basis measurement transforms the linear graph into a non-linear graph. One X gate as an byproduct, and an additional Hadamard gate needs to be applied to a neighboring qubit of the measured target. While the target qubit of the byproduct X gate does not affect the overall state but fixes the phase, the target qubit of the Hadamard gate directly affects the graph as in Figure 2.28(c).

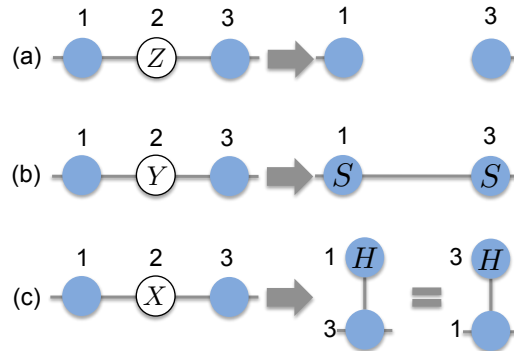


Figure 2.28: Topological transition by measurements on 1D cluster states

Similar to the 1D graph, performing measurements on a 2D cluster states affect the graph in a 2-dimensional manner. The Z-basis measurement performed on an arbitrary qubit will simply result in a new topology without the measured qubit and its links as in Figure 2.29(a). The Y-basis measurement also removes the measured qubit but leaves additional complementary links between the neighbors of the measured qubit

(Figure 2.29(b)). The output topology after X-basis measurement differs according to the feedforward target, which is a neighbor qubit of the measurement target (filled with gray color in 2.29(c)). After the measurement, new complementary links are formed between the neighbors of the feedforward targeted qubit and the neighbors of the measured qubit, between the mutual neighbors of the feedforward targeted and the measured qubit, and between the feedforward targeted qubit and the neighbors of the measured qubit. Similar to other measurements, the measured qubit is removed and its links will be disconnected from other qubits.

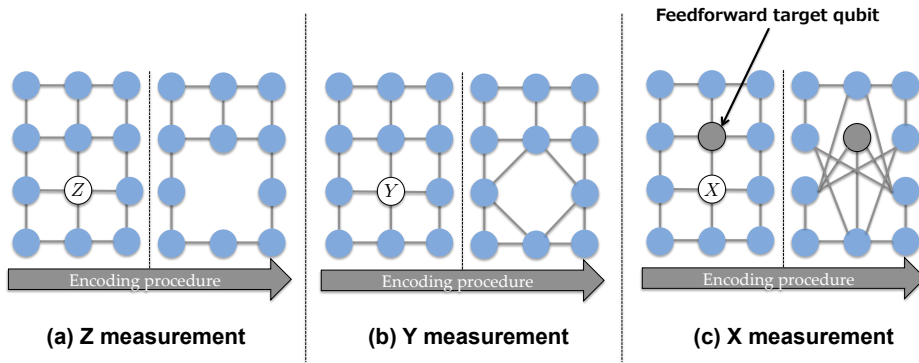


Figure 2.29: Topological transition by measurements on 2D cluster states

Chapter 3

Current State of Experimental Work

3.1 Satellite-based entanglement distribution over 1200 kilometers

Recently, in 2017, China achieved the longest ever entanglement distribution using their quantum satellite, Micius, which was designed to produce two separate photons with entangled polarizations as $|\Psi^+\rangle = \frac{1}{\sqrt{2}}(|01\rangle + |10\rangle)$ [19]. Pairs of photons are beamed down to earth under a pump power of 30 mW, with a rate of 5.9 million entangled pair second with a fidelity of 0.907 ± 0.007 , and measured at ground stations separated by 1203km. Overall the experiment succeeded in distributing 1.1 entanglement per second in average across over 1203km distance with a fidelity 0.869 ± 0.085 .

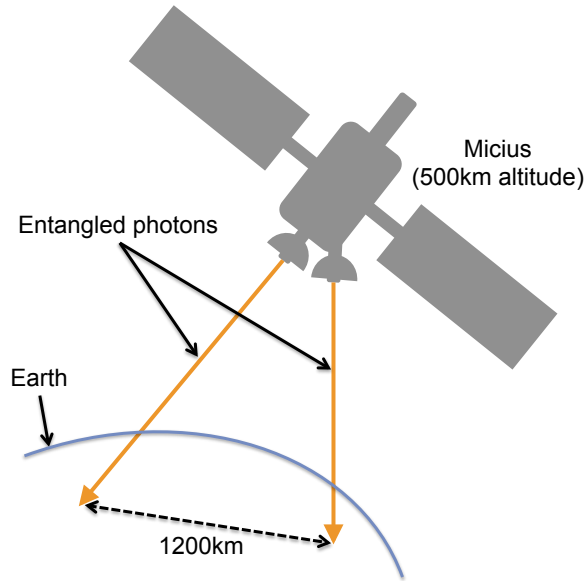


Figure 3.1: Chinese satellite beaming down entangled photons to earth

3.2 Photon pair experiment and the violation of CHSH inequality

One of the Bell inequalities, known as CHSH inequality, allows us to mathematically prove that quantum mechanics cannot be explained by local hidden variables theory. In a classical Newtonian physics, the correlations between outcomes of measurements on distant particles must satisfy an inequality $|S| < 2$ (S is the correlation between measurement outcomes). Since quantum mechanics do not obey locality and realism, the same experiment on entangled particles violates the inequality and result in a different boundary $2\sqrt{2} \approx 2.82843$ - known as *Tsirelson's bound*.

In 2015, Poh et al. experimented the correlation of maximally entangled photon polarization, and observed $S = 2.82759 \pm 0.00051$, which is very close to Tsirelson's bound $S - 2\sqrt{2} = 0.00084 \pm 0.00051$ [20].

In the same year, Hensen et al succeeded in demonstrating a loophole-free Bell inequality violation using electron spins separated by 1.3km [21] - previously reported experiment results required extra assumptions which caused in loopholes [22, 23, 24, 25]. Using entangled electron spins of an estimated fidelity $F = 0.92 \pm 0.03$, 245 trials of direct CHSH-Bell inequality test have been performed, and observed $S = 2.42 \pm 0.20$.

3.3 Experimental generation of cluster states

In 2013, Lanyon et al. demonstrated principles of MBQC using deterministically generated cluster states of up to 7 qubits using trapped calcium ions [26]. For testing single-qubit measurements, a linear cluster state of 4 qubits have been generated using a laser pulse sequence lasting $300\mu\text{s}$. The full density matrix had been reconstructed via quantum state tomography, and the observed fidelity is 0.841 ± 0.006 . In the experiment, a range of measurement combination has been implemented to implement different rotations. The fidelity after the measurements is 0.92 ± 0.01 in average. Moreover, 5 different cluster states up to 7 qubits has been tested, which includes the linear cluster state and other simple 2D graphs, and all of the states violated the Bell inequality, which implies that no local hidden variable model can explain the experimental result.

In 2013, Yokoyama et al. succeeded in deterministically generating a large scale continuous-variable cluster state by multiplexing the light modes in the time domain. The generated cluster state contains more than 10,000 entangled modes, each of them individually addressable [27]. They have also developed an efficient MBQC scheme based on sequential applications of quantum teleportation for the generated cluster state in particular.

In 2016, Schwartz et al. implemented a scheme for deterministic generation of long strings of entangled photons in a cluster state [28]. A photonic cluster state is considered to be suitable for quantum computing, as the use of photon polarization as a qubit facilitates high fidelity single qubit measurements. The demonstration follows Lindner and Rudolph's proposal [29], where in this case an dark exciton spin is entangled with the photon polarization that is emitted by its own excitation. The timed re-excitation

emits more photons, leading to a string of 1D cluster state. The prototype succeeded in producing strings of a few hundred photons in which entanglement persists over 5 sequential photons.

Chapter 4

Related Work

4.1 Classical Network Coding

Classical network coding, introduced by Ahlswede, Cai, Li, and Yeung [1], is a notably simple, yet important technique for resolving resource contention over networks. A node in a computer network generally behaves as a switch, responsible for relaying a received packet to one or more neighboring nodes by replicating the information. However, scarce network resources result in packet congestion, and may significantly affect applications that rely on the connectivity. In order to mitigate this issue, network coding treats each node in a network as an encoder instead of a switch.

The simplest example of network coding can be represented on a butterfly network as shown in Figure 4.1. In this example, there are two source nodes S_1 and S_2 with the goal delivering messages X and Y to their target nodes t_2 and t_1 respectively. Here, each message is assumed to be 1 bit of data, and all directed channels have a limited capacity of 1 bit per second. With a general routing protocol, no matter what path is chosen for each connection, the two paths must overlap somewhere, resulting in contention for access to one link.

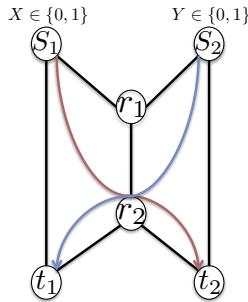


Figure 4.1: Resource contention over Butterfly network

Therefore, the link between the intermediate resource nodes r_1 and r_2 becomes a bottleneck. One possible solution for such problem may be the use of time division multiplexing, which uses two cycles to complete the message transmission. One message transmission can be finished first, and the second transmission can be completed afterwards, which may result in long delays.

On the other hand, network coding can resolve this bottleneck problem within one cycle by linearly combining the incoming messages and transmitting them as one message (see Figure 4.2). Source node S_1 sends its message towards the target node t_1 and to the resource node r_1 . Similarly, source node S_2 forwards its message towards the target node t_2 and the resource node r_1 . The resource node r_1 then processes the incoming messages, using XOR operation to linearly combine the messages, and forwards the newly created message to both target nodes via r_2 . At the end, each node can reconstruct their desired message by decoding the linearly combined message, using XOR operation between the other message directly sent from the source node to the target node. Therefore, network coding can achieve a throughput of two messages per second.

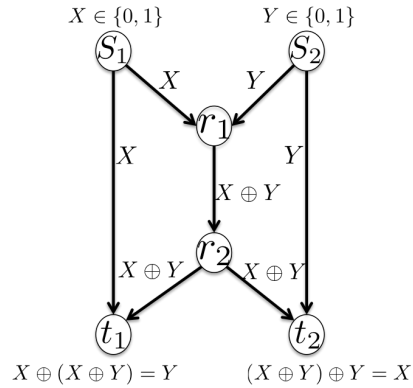


Figure 4.2: Network coding on a butterfly network

Network coding may be useful in multicast, wireless sensor networks, satellite communication and Peer-to-Peer file sharing.

4.2 Multiplexing using Entanglement Swapping

Alternative implementation methods, such as Buffer-Space Multiplexing and Time-Division Multiplexing, are often used for comparing performance between network coding.

4.2.1 Buffer-Space Multiplexing

If the bottleneck link has enough resources, the buffer-space multiplexing divides the available qubit memory space and assigns part of it to each flow. This allows multiple links to be established simultaneously within once cycle, if resource is abundant. The simplified model is shown in Figure 4.3

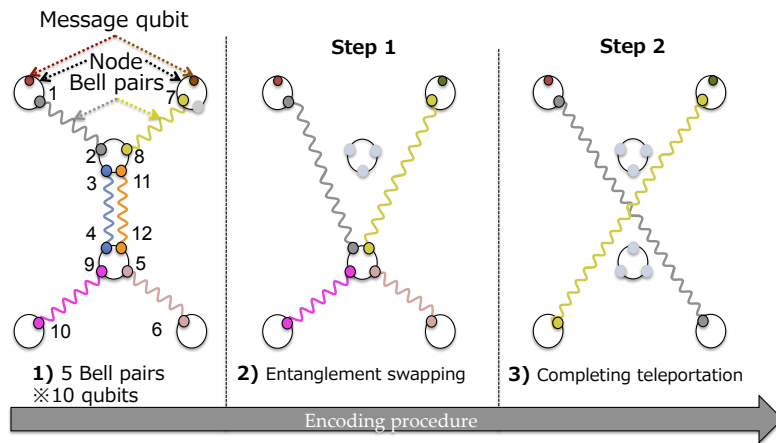


Figure 4.3: Simplified model of buffer-space multiplexing using entanglement swapping. The resource in the center link must be used shared.

4.2.2 Time-Division Multiplexing

The time-Division Multiplexing in quantum networking can be accomplished by entanglement swapping. For a pictorial model of ES, see Figure 4.4.

In this model, qubit 3 and qubit 4 at the bottleneck link will be shared among nodes for completing the whole transmission process. The bottleneck link will be used to complete one transmission first, and then will be regenerated to finish up the second transmission. It is almost the same as Buffer-Space Multiplexing, but two cycles are needed in order to complete the whole process.

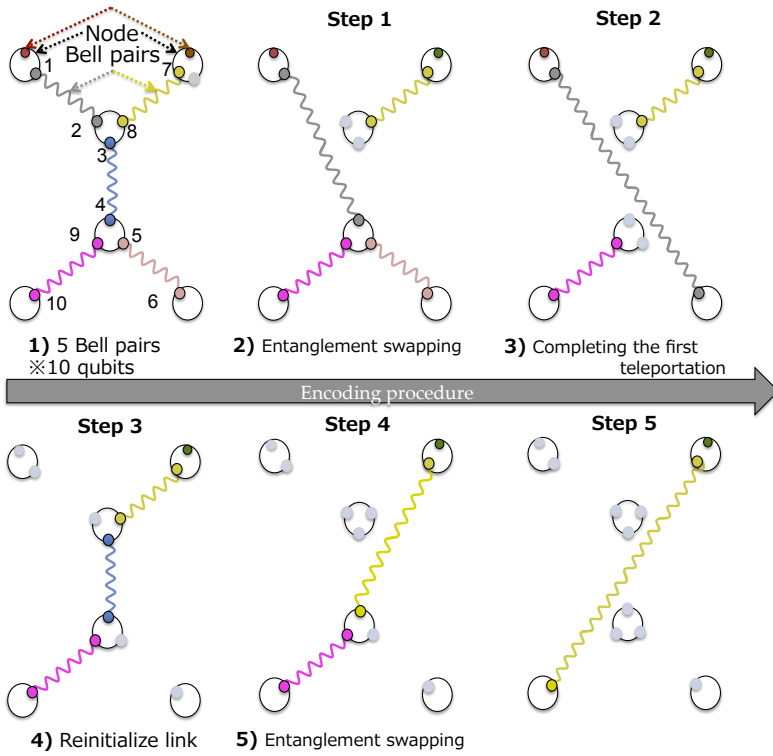


Figure 4.4: Simplified model of time-division multiplexing using entanglement swapping. The center link must be used twice.

4.3 Quantum Network Coding

Quantum network coding also aims to send multiple messages (quantum information) from multiple sources to multiple destinations simultaneously. Unlike classical information, quantum information forbids copying an unknown quantum state - *no-cloning theorem*. Therefore, although the goal still remains the same for classical and quantum network coding, the physical approach for accomplishing the goal differs from each other.

In 2006, Hayashi et al. showed that the communication fidelity is upper bounded by $F_{output} < 0.983$, when simultaneously transmitting messages (quantum information) over a butterfly network via quantum network coding without free classical channels [30]. Furthermore, in 2007, Leung et al. generalized this impossibility to several network types including the butterfly network, and concluded that perfect quantum network coding is impossible even with asymptotically perfect transmission [31]. Later on, Kobayashi et al. showed that perfect quantum network coding can be accomplished whenever free classical channels are available, for any graph shape that is solvable by classical network coding [32, 33, 34]. All work assumed that qubits have pure states.

4.3.1 Quantum Network Coding for Repeater networks

In 2012, Satoh et al. developed a more simplified quantum network coding protocol for quantum repeater networks (QNC) [4]. Previously introduced quantum network coding protocols [30, 31, 32, 33, 34, 35] directly encode on the message qubits, however, QNC avoids any operation to the message qubits in the middle of the protocol. Performing complex gate operations directly to the message qubits degrades the qubit state, and performing purification to the message after a complex encoding may not be easy. Instead, QNC focuses on creating 2 crossing-over paths by using the Bell pairs shared across quantum repeaters with a goal to lowering the protocol complexity and to improve the communication fidelity.

As shown in the QNC encoding procedure in Figure 4.5 and the corresponding circuit in Figure 4.6, the network is assumed to have 7 Bell pairs shaping a butterfly graph - Classical channels are assumed to be undirected and have unlimited capacity. A six-step procedure takes us from the seven separate Bell pairs to two end-to-end Bell pairs via QNC.

$$|\Psi_0\rangle = |\Phi_{0,1}^+\rangle |\Phi_{2,3}^+\rangle |\Phi_{4,5}^+\rangle |\Phi_{6,7}^+\rangle |\Phi_{8,9}^+\rangle |\Phi_{10,11}^+\rangle |\Phi_{12,13}^+\rangle \quad (4.1)$$

Using the given resources, the first step of the protocol connects a particular set of Bell pairs to generate two 3-qubit GHZ states.

$$[Step1(Connection)] |\Phi_{0,1}^+\rangle |\Phi_{2,3}^+\rangle |\Phi_{4,5}^+\rangle |\Phi_{6,7}^+\rangle = |GHZ_{0,1,3}\rangle |GHZ_{4,5,7}\rangle \quad (4.2)$$

Therefore, the overall system after Step 1 can be described as:

$$|\Psi_1\rangle = |GHZ_{0,1,3}\rangle |GHZ_{4,5,7}\rangle |\Phi_{8,9}^+\rangle |\Phi_{10,11}^+\rangle |\Phi_{12,13}^+\rangle \quad (4.3)$$

The bottleneck link is manipulated to bridge the GHZ states to the left and right as a parity qubit as in Step 2.

$$\begin{aligned} |\Psi_2\rangle &= \frac{1}{2}(|0_00_10_30_40_50_7\rangle + |1_01_11_31_41_51_7\rangle) |0\rangle_9 \otimes |\Phi_{10,11}^+\rangle |\Phi_{12,13}^+\rangle \\ &\quad + \frac{1}{2}(|0_00_10_31_41_51_7\rangle + |0_00_10_31_41_51_7\rangle) |1\rangle_9 \otimes |\Phi_{10,11}^+\rangle |\Phi_{12,13}^+\rangle \end{aligned} \quad (4.4)$$

In Step 3, FANOUT operation is applied to the parity qubit, which is qubit 9.

$$\begin{aligned} |\Psi_3\rangle &= \frac{1}{2}(|0_00_10_30_40_50_7\rangle + |1_01_11_31_41_51_7\rangle) |000\rangle_{9,11,13} \\ &\quad + \frac{1}{2}(|0_00_10_31_41_51_7\rangle + |0_00_10_31_41_51_7\rangle) |111\rangle_{9,11,13} \end{aligned} \quad (4.5)$$

In Step 4, CNOT operation will be applied to qubits at both target nodes.

$$\begin{aligned} |\Psi_4\rangle &= \frac{1}{2}(|0_00_10_30_40_50_7\rangle + |1_01_11_31_41_51_7\rangle) |000\rangle_{9,11,13} \\ &\quad + \frac{1}{2}(|0_01_10_31_40_51_7\rangle + |1_00_11_30_41_50_7\rangle) |111\rangle_{9,11,13} \end{aligned} \quad (4.6)$$

In Step 5, parity qubits at both target nodes are removed from the graph by measurement.

$$\begin{aligned} |\Psi_5\rangle &= \frac{1}{2}(|0_00_10_30_40_50_7\rangle + |1_01_11_31_41_51_7\rangle) |0\rangle_9 \\ &\quad + \frac{1}{2}(|0_01_10_31_40_51_7\rangle + |1_00_11_30_41_50_7\rangle) |1\rangle_9 \end{aligned} \quad (4.7)$$

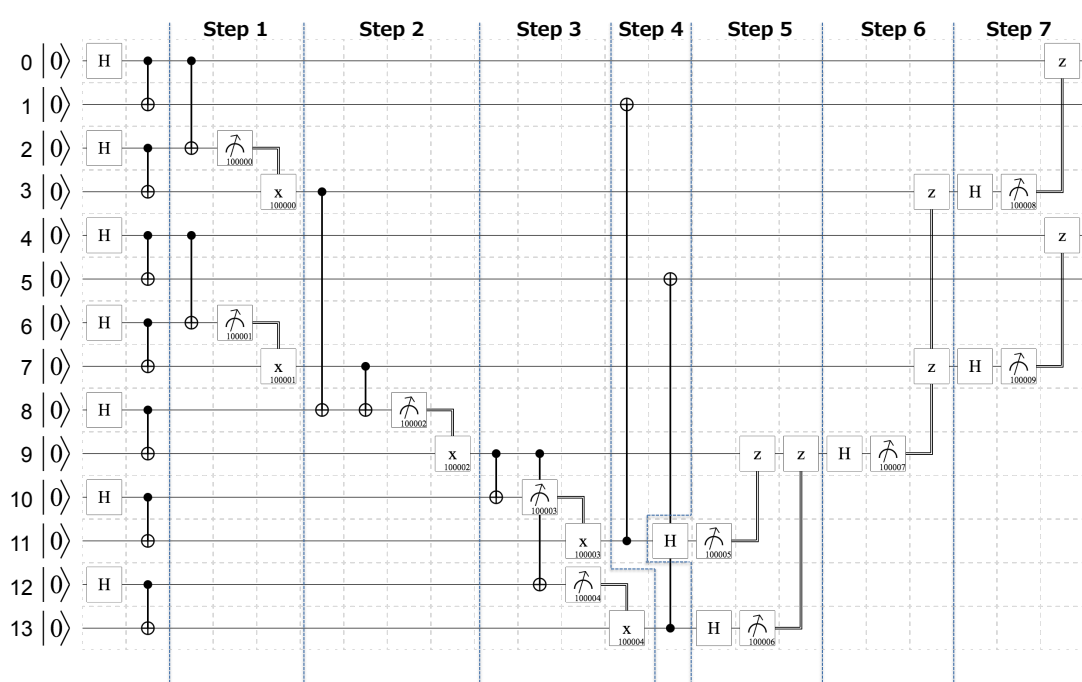
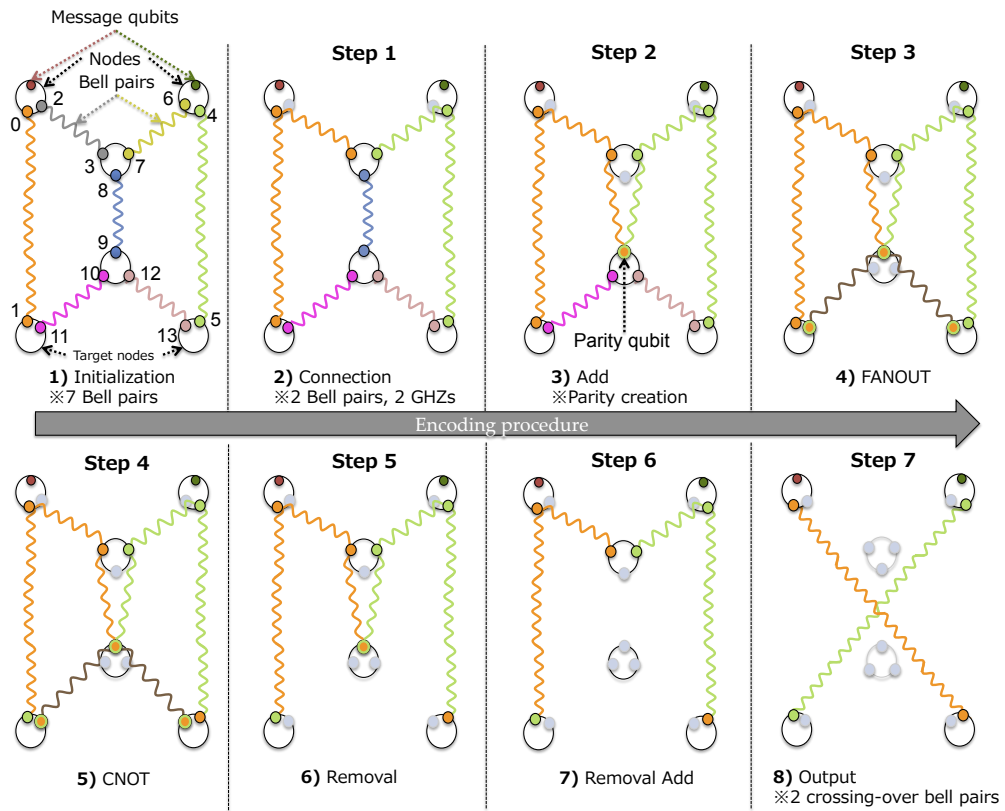
The parity qubit at the bottleneck link is removed in Step 6.

$$\begin{aligned} |\Psi_6\rangle &= \frac{1}{2}(|0_00_10_30_40_50_7\rangle + |1_01_11_31_41_51_7\rangle) \\ &\quad + \frac{1}{2}(|0_01_10_31_40_51_7\rangle + |1_00_11_30_41_50_7\rangle) \end{aligned} \quad (4.8)$$

In the last step, the remaining qubits at the bottleneck node is removed from the graph to form 2 crossing-over Bell pairs.

$$\begin{aligned} |\Psi_6\rangle &= \frac{1}{2}(|0_00_10_40_5\rangle + |1_01_11_41_5\rangle) \\ &\quad + \frac{1}{2}(|0_01_11_40_5\rangle + |1_00_10_41_5\rangle) \\ &= |\Phi_{0,5}^+\rangle \otimes |\Phi_{1,4}^+\rangle \end{aligned} \quad (4.9)$$

This completes the sequence and results in two end-to-end Bell pairs, which can be used to teleport the message qubit from source to destination directly.



Later in 2016, Satoh et al. studied QNC under noisy conditions using Monte-Carlo

simulation. The paper concluded that ES tolerates about twice the local error rate of QNC. Each operation in QNC is ordered in time, therefore, qubit dependencies worsen the quantum circuit depth. Due to the high circuit complexity, local operation accuracies tend to have a larger impact on the output fidelity compared to initial entangled resource fidelity. Moreover, even with perfect local gates, the output fidelity drops below $F_{output} < 0.5$ when the initial Bell pairs have fidelity $F_{input} < 0.90$. While ES offers higher communication fidelity, QNC reduces the required cycle, and therefore provide benefit if network resources are limited or if higher communication speed is demanded.

4.3.2 MBQC

Performing X-measurements on the bottleneck qubits of a butterfly cluster state will result in 2 crossing-over cluster states [36]. For a simplified model of this scheme, see Figure 4.7. Although this algorithm seems to be a lot simpler compared to QNC, one should be reminded that creating a cluster state requires interfering of all qubits that are involved, thus, it is not feasible to directly create a multi-qubit cluster state using qubits that are far apart.

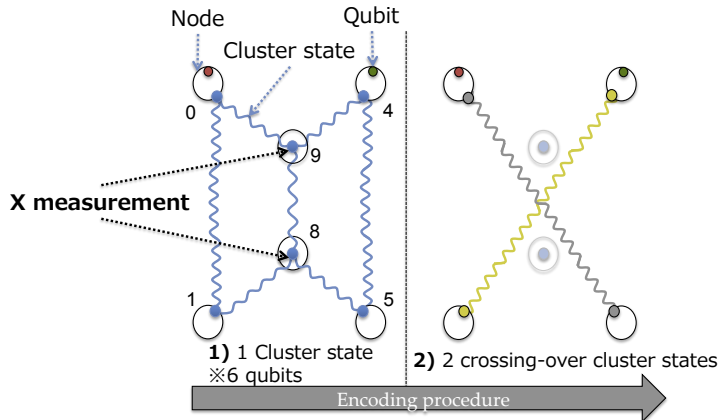


Figure 4.7: Visualized encoding procedure of network coding on cluster state

In the next chapter, this thesis introduces a step-by-step procedure of the newly developed protocol, which is based on QNC and MBQC. With a similar initial setting to QNC, the developed protocol manipulates the shared resources to form a 6-qubit cluster state through local operations, and perform X-basis measurements to the bottleneck link.

Chapter 5

Protocol Design

5.1 MQNC Protocol

QNC is practical as it can be implemented over quantum repeater networks and used for long distance communications. Nevertheless, the encoding procedure is based on the classical counterpart which results in many qubit dependencies, lengthening the circuit depth, and therefore adversely affecting the communication fidelity. While the benefit of MBQC comes from the simplicity of implementation, the scheme for MBQC can only be directly applied to a system area network. The main reason for this comes from the difficulty of creating a multi-qubit cluster state using qubits that are far apart, as cluster state generation requires interfering of all qubits that are involved.

The proposed protocol, MQNC, takes advantage of both QNC and MBQC using local operations and classical communication (LOCC) and the Bell pairs created on repeater network links. Unlike the other network coding schemes for quantum communication that directly encode on qubits to combine messages (based on the classical algorithm), and QNC that uses CNOT operations (which is the quantum equivalent of XOR) to create parities on quantum channels (also based on classical network coding), MQNC focuses on generating 2 crossing-over paths, which partially takes the idea of QNC but without a single use of CNOT gates (not based on classical network coding). The basic idea of MQNC is to create a 6-qubit butterfly cluster state from the 7 shared entangled pairs, and to treat the generated state as a resource state for network level MBQC, which allows us to topologically achieve the same goal as QNC. The developed protocol's simplified model is shown in Figure 5.1. Entangled states across nodes are assumed to be ready, and therefore the link-timing architecture [37, 38] for entanglement distributions has not been taken into consideration in this thesis. As shown, the encoding procedure for MQNC can be divided into 3 major steps. The first step is the initialization part, where entangled resources between quantum repeaters are prepared. The second step is the creation of the butterfly-shaped 6-qubit cluster state using only LOCC and the given resources prepared in the first step. The last step completes the measurement-based quantum network coding by creating 2 crossing-over independent cluster states out of the butterfly graph.

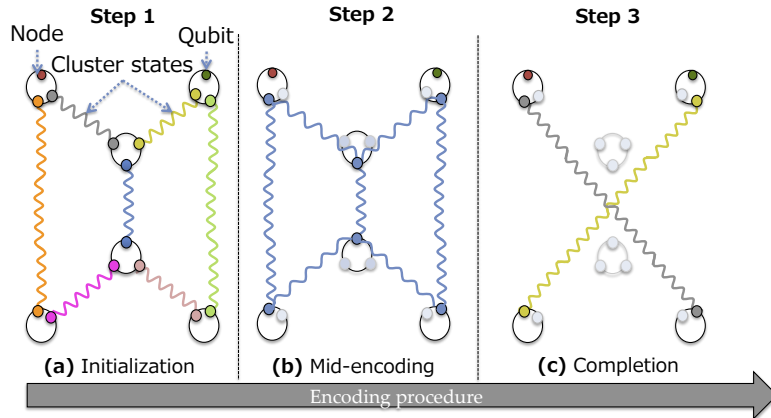


Figure 5.1: Flow of MQNC encoding

5.1.1 1st Step: Initialization of Shared Resources

The first step of the protocol requires a preparation of seven independent 2-qubit cluster states across quantum repeaters. A 2-qubit cluster state can be generated by the following circuit as in Figure 5.2(a) with a simplified model of the input and output visualization shown in Figure 5.2(b). Notice that a cluster state can be generated from a Bell pair by applying an additional Hadamard gate to qubit 2. However, from the relation between the CZ gate and the Controlled-NOT gate (for details, refer to Figure 2.11), a cluster state can be created effectively by applying Hadamard gates to both qubits beforehand. Most importantly, the generation of a Bell pair and a 2-qubit cluster state requires the same cost in terms of circuit depth (experimental methods are introduced in Chapter 4). All seven cluster states are prepared with the same procedure independently.

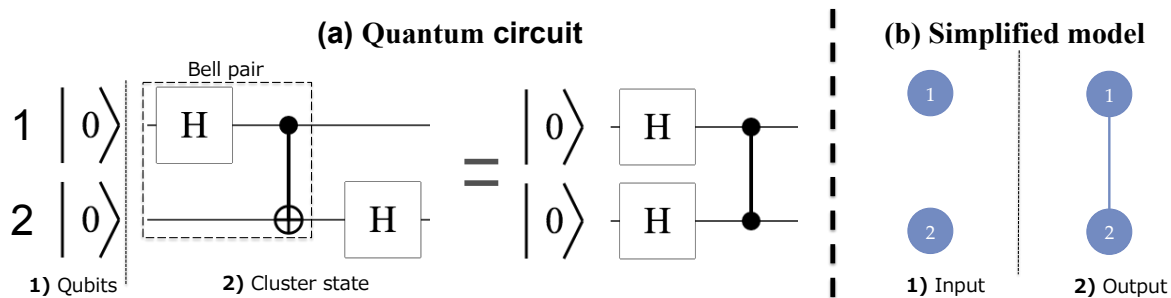


Figure 5.2: 2-qubit cluster state generation (a) Quantum circuit of 2-qubit cluster state generation (b) Simplified model of 2-qubit cluster state generation

The output of the above circuit can be calculated using Dirac notation:

$$\begin{aligned}
& \Lambda_{1,2}(Z)H_2H_1|0_10_2\rangle \\
&= \Lambda_{1,2}(Z)H_2\frac{1}{\sqrt{2}}(|0_10_2\rangle + |1_10_2\rangle) \\
&= \Lambda_{1,2}(Z)\frac{1}{2}(|0_10_2\rangle + |1_10_2\rangle + |0_11_2\rangle + |1_11_2\rangle) \\
&= \frac{1}{2}(|0_10_2\rangle + |1_10_2\rangle + |0_11_2\rangle - |1_11_2\rangle) \\
&= \frac{1}{\sqrt{2}}(|0_1+2\rangle + |1_1-2\rangle)
\end{aligned} \tag{5.1}$$

As shown in equation 5.2, the circuit outputs a cluster state, entangling two qubits. The circuit output can also be tracked by using stabilizers. Each qubit has a state $|0\rangle$, where the overall initial state can be described by stabilizers Z_1 and Z_2 . The Hadamard gate then swaps the $|0\rangle$ state and $|+\rangle$ state. Therefore, applying Hadamard gates to each qubit and performing a CZ gate between them will result in new stabilizers X_1Z_2 and Z_1X_2 . The flow of stabilizers on the quantum circuit is described in Figure 5.3.

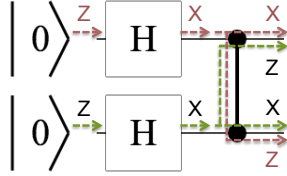


Figure 5.3: Stabilizer flow of 2-qubit cluster state generation circuit

5.1.2 2nd Step: Creating 6-qubit cluster state

Adding another qubit to a pre-generated cluster state can be accomplished by implementing another CZ gate between the qubits, as in Figure 5.4. Here, qubit 3 is added to another pre-generated 2-qubit cluster state of qubit 1 and qubit2, resulting in a linearly entangled cluster state of all three qubits.

$$\begin{aligned}
& \Lambda_{2,3}(Z)H_3|0_3\rangle \frac{1}{\sqrt{2}}(|0_1+2\rangle + |1_1-2\rangle) \\
&= \Lambda_{2,3}(Z)\frac{1}{\sqrt{2}}(|0_10_2+3\rangle + |1_1-2+3\rangle) \\
&= \frac{1}{2}(|0_10_2+3\rangle + |0_11_2-3\rangle + |1_11_2+3\rangle + |1_11_2-3\rangle)
\end{aligned} \tag{5.2}$$

Besides just a single qubit, but an independent cluster state can also be connected to another cluster state through the same procedure. Removing a qubit from a graph is sometimes helpful. The excision of an intermediate qubit of a linearly entangled cluster state can be accomplished by the use of Y-basis measurement with two classical

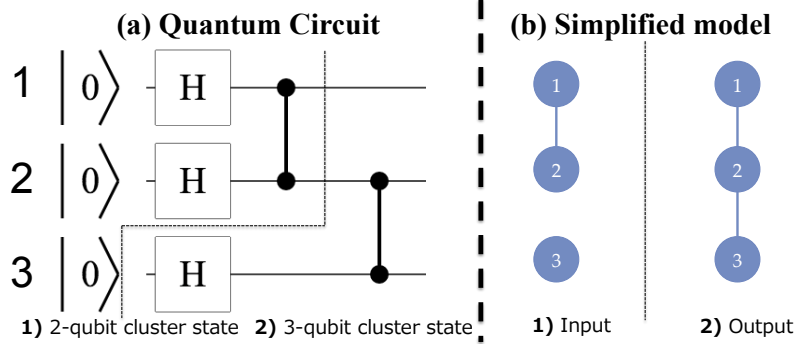


Figure 5.4: 3-qubit linear cluster state generation (a) Quantum circuit of linear 3-qubit cluster state generation (b) Simplified model of linear 3-qubit cluster state generation

Table 5.1: Stabilizers after the Y measurement

qubits		
Stabilizer 1	X_1	Z_2
Stabilizer 2	Z_1	Y_2
Stabilizer 3		-1^{t_3}
	Z_2	$-1^{t_3} Y_4$

feedforward operations. The stabilizers of the system after measuring qubit 3 are described in Table 5.1.

The variable t_3 is the measurement outcome, either 0 or 1, of qubit 3. Depending on the measurement result, two phase operations are performed to the neighboring qubits of the measured target. Unlike other byproduct operators that show up in this thesis, a Y measurement on a cluster state always requires the phase of residual system to be corrected, by either S gate or S^\dagger gate depending on the measurement result.

In this example, qubit 3 is measured with respect to the Y-basis, and the graph is directly connected up to the phase operations to qubit 2 and qubit 4 as a byproduct. For details regarding the topological transition, see to Figure 5.5.

A star graph known as $K_{1,3}$, also known as the claw graph, is a subgraph of a butterfly network. The simplest claw cluster state composed of 4 qubits can also be created with similar procedure as shown in Figure 5.6. CZ gate is performed between qubit 2 and qubit 3, which is the intermediate qubit of the linear 3-qubit cluster state, and qubit 5 which is the edge of a 2-qubit cluster state. Afterwards, qubit 5 is removed from the graph using Y-basis measurement.

With all the introduced techniques above, 6-qubit butterfly cluster state can be generated using the seven initialized entangled resources. For simplicity, the second step of MQNC is divided into further sub-steps as in Figure 5.7. The corresponding circuit is shown in Figure 5.8.

In Step 1, which is the initialization part of the protocol, seven independent cluster states are generated using the fourteen qubit resources across quantum repeaters. Each cluster state is generated using the technique in Figure 5.2. Step 2.1 uses the initialized

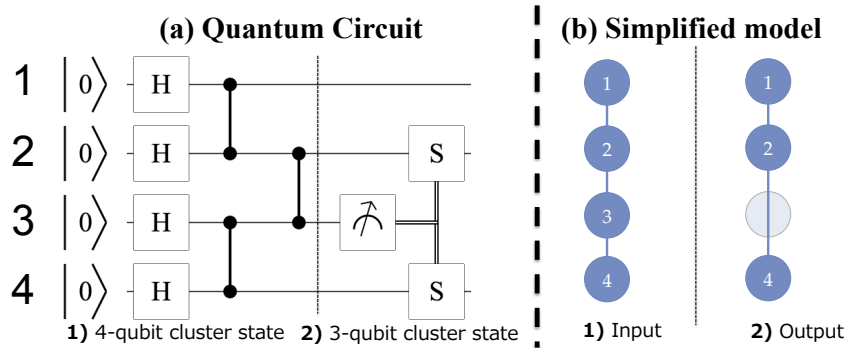


Figure 5.5: Y measurement performed on linear cluster state. (a) Quantum circuit of linear 3-qubit cluster state generation using Y measurement. (b) Simplified model of linear 3-qubit cluster state generation using Y measurement.

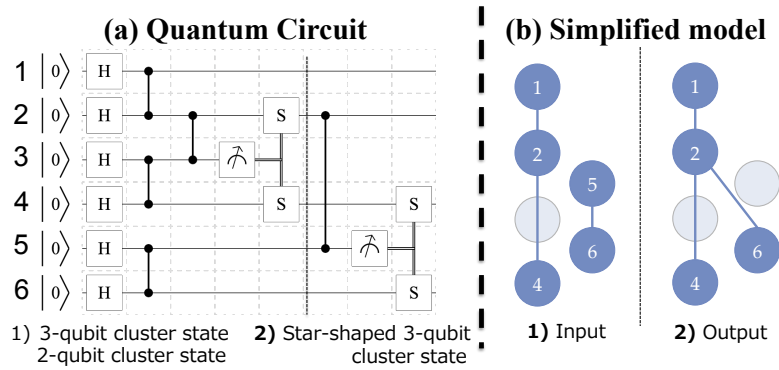


Figure 5.6: 4-qubit star-shaped cluster state (a) Quantum circuit of 4-qubit star-shaped cluster state generation (b) Simplified model of linear 4-qubit star-shaped cluster state generation

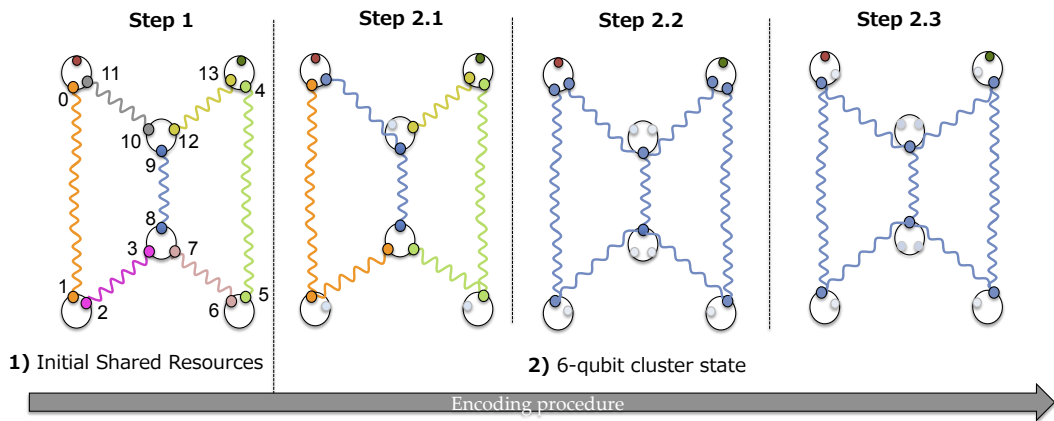


Figure 5.7: MQNC step2

resources to linearly connect qubits as in Figure 5.5, resulting in three 3-qubit linear cluster state and one 2-qubit cluster state. In the next step, Step 2.2, qubits at the bottle neck node are connected together, shaping a non-linear cluster state to bind the

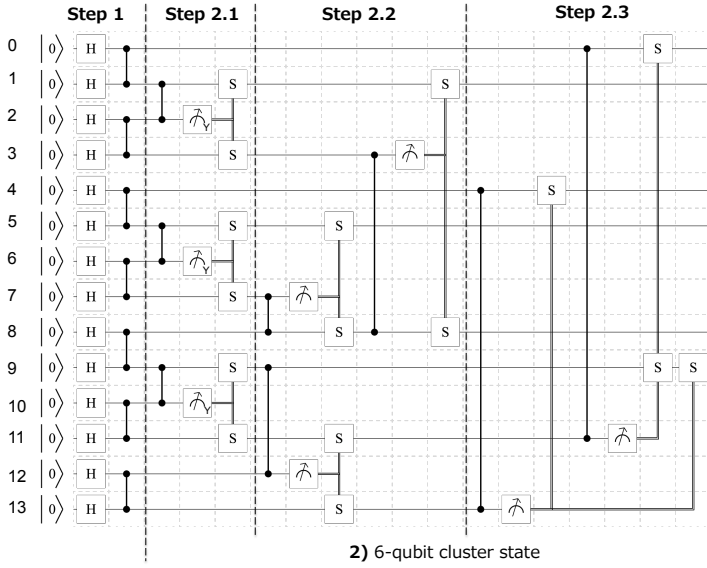


Figure 5.8: MQNC step2 circuit

neighboring nodes - using the technique shown in Figure 5.6. At last, the remaining two qubits at the left-top (qubit 0 and qubit 11) and right-top (qubit 13 and qubit 4) are entangled and the unwanted qubits are removed from the graph to shape a proper butterfly network.

5.1.3 3rd Step: Creating 2 crossing-over cluster states

Once a butterfly cluster state (see Figure 4.7) is prepared, the next thing to do is to create 2 crossing-over cluster states. This can be accomplished by applying X-basis measurements on the bottleneck qubits (qubit 8 and qubit 9). As there are 6 qubits involved in the system, 6 stabilizers are required to represent the butterfly cluster state. Details are shown below in Table 5.2. After the X measurements on qubit 8 and qubit 9, stabilizers change to the following set as in Table 5.3.

Table 5.2: Stabilizers of a butterfly cluster state : pre-measurement

	qubits					
Stabilizer 1	X_0	Z_1			Z_9	
Stabilizer 2	Z_0	X_1	Z_8			
Stabilizer 3		Z_1	X_8	Z_9		Z_5
Stabilizer 4	Z_0		Z_8	X_9	Z_4	
Stabilizer 5				Z_9	X_4	Z_5
Stabilizer 6		Z_8			Z_4	X_5

This implies that up to the measurement result, the phase of the quantum state may change. In order to fix the phase to a desired state, either Z gates or X gates

Table 5.3: Stabilizers of 2 crossing-over cluster states : post-measurement

	qubits			
Stabilizer 1	X_0	-1^{t_8}		Z_5
Stabilizer 2		X_1	-1^{t_9}	Z_4
Stabilizer 3		Z_1	-1^{t_8}	X_4
Stabilizer 4	Z_0		-1^{t_9}	X_5

can be used. When using Z gates, two Z gates are applied to qubit 0 and qubit 4 as a byproduct of qubit 8 measurement. Similarly, two Z gates are applied to qubit 1 and qubit 5 as a byproduct of measurement on qubit 9. Alternatively, one can achieve the same goal by performing X gates to qubit 0 and qubit 4 as a byproduct of measuring qubit 9, and to qubit 1 and qubit 5 as a byproduct of measuring qubit 8. In this thesis, MQNC assumes to perform X gates as byproduct operators since it requires less time due to shorter distance for classical packet transmission. A simple full quantum circuit of MQNC is as shown below in Figure 5.9.

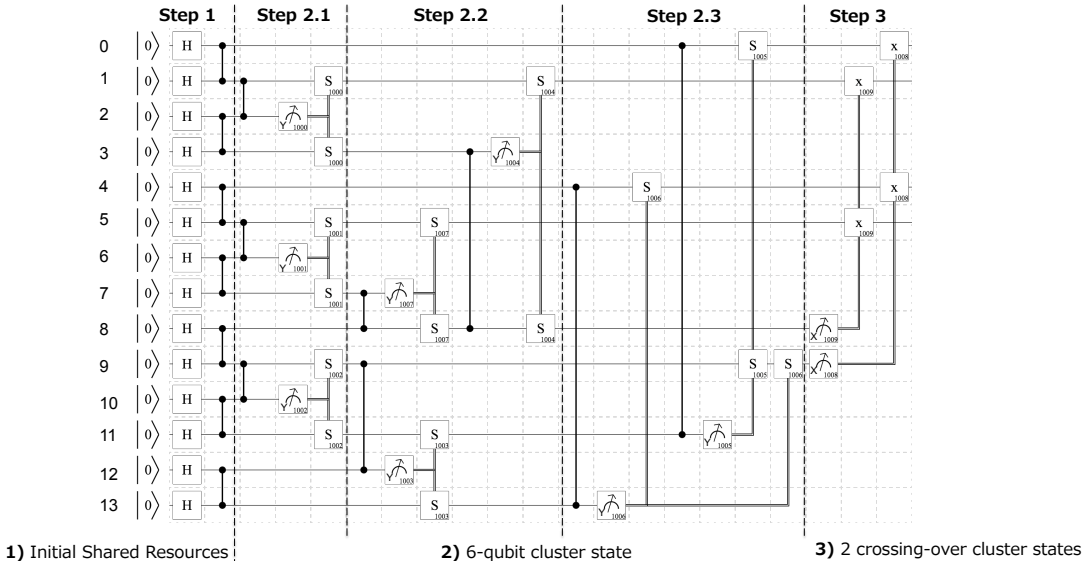


Figure 5.9: Simple circuit of MQNC

5.1.4 Compressing Quantum Circuit of MQNC

Measurement operations, Phase gates and CZ gates commute. Therefore, the order of applying such operations can be changed. In detail, measuring a particular qubit of a cluster state and connecting the resulting state to another cluster state using CZ gate equates to connecting the two cluster states beforehand and measuring the qubit later. Taking full advantage of this gate commutativity allows us to parallelize some encoding operations, which contributes to reducing the circuit depth.

Instead of strictly following the procedure of the above circuit in Figure 5.9, as operations do not depend on each other, all CZ gate operations can be applied in a parallel manner at the beginning of the protocol, and measuring qubits can be done afterwards. The compressed circuit for MQNC is now as shown in Figure 5.11 with a simple representation as in Figure 5.10. In the end, MQNC has achieved a 52% reduction of circuit depth compared to QNC.

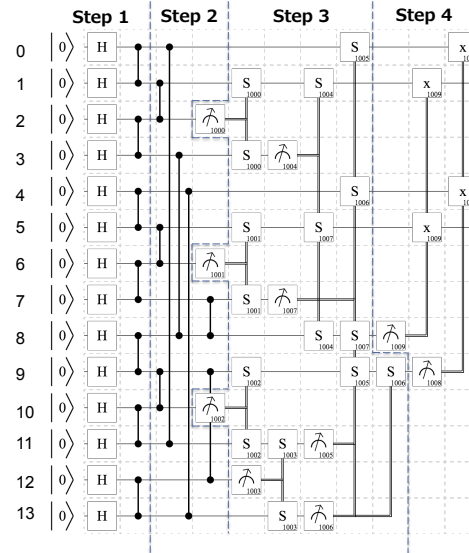


Figure 5.10: Compressed circuit of MQNC

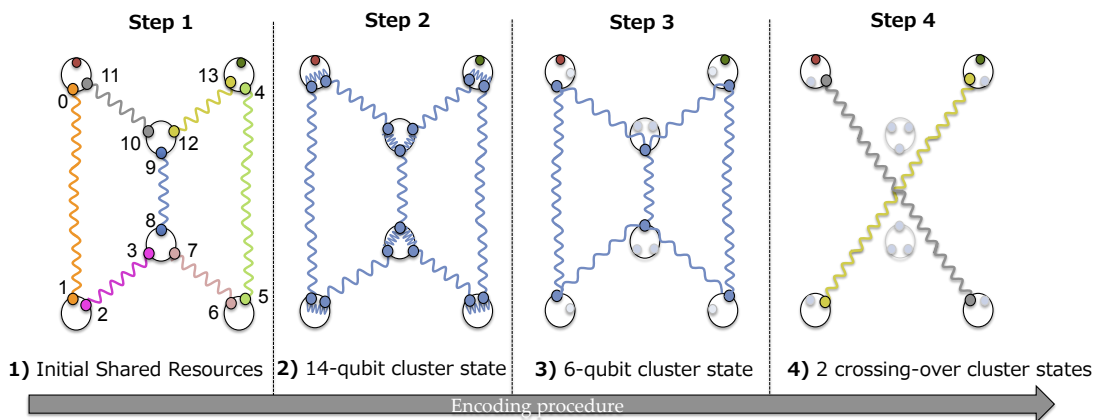


Figure 5.11: Representation of compressed MQNC encoding

Chapter 6

Evaluation

The behavior of the proposed protocol has been studied through Monte-Carlo simulation by tracking error propagations classically with various error sources. Results of the simulations are compared statistically with other alternative implementation methods, which includes buffer-space multiplexing using entanglement swapping (ES) and Quantum Network Coding for Repeater Networks (QNC) (for details, see Related Work).

The program that has been used in this thesis is an extended version of Doctor Shota Nagayama's code that has been originally developed for his Doctoral thesis in 2016 [39]. The total length of the program files differs according to the simulation settings, but for MQNC in particular, approximately 3100 lines of code have been used.

6.1 Environment

The development environment is summarized in Table 6.1.

Table 6.1: Development environment

Operating system	OSX Yosemite 10.10.4
Processor	2 GHz Intel Core i7
Memory	8GB
Launage	Python 3.6.1

The developed program had been run in a different environment with a higher computation power as summarized in Table 6.2. Each simulation lasted for 1 to 2 hours.

Table 6.2: Simulation environment

Operating system	CentOS 6.9
Processor	3.50 GHz Intel Core i7
Memory	32GB
Launage	Python 3.6.1

6.2 Common simulation settings

Operations in the same category (e.g. single-qubit gates) are assumed to share the exact same error rate. That is to say, if one H gate has an error rate of ε , all other single-qubit gates also share the same error rate. Noisy operations in the simulation include:

1. Single qubit gates
 - (a) Z gate
 - (b) X gate
 - (c) H gate
 - (d) S gate
2. Controlled gates
 - (a) CZ gate
 - (b) CNOT gate
3. Measurements
 - (a) Z measurement
 - (b) X measurement
 - (c) Y measurement
4. Qubit memories
 - (a) I gate
5. Initial resource
 - (a) Qubit initialization
 - (b) Bell pair initialization
 - (c) 2-qubit cluster state initialization

The first two error sources are the gate errors, which include the single-qubit gate error and the controlled gate error. The third error source is the error caused by faulty qubit measurement. An error on the measured qubit may also cause a faulty measurement result, which propagates to other qubits through misleading byproduct operations. The fourth error is the memory error, which simulates the decoherence on qubits that interferes and affects the qubit state; as a qubit memory is not supposed to anything to the state, it is often described as the identity gate. The last error source is the initial resource error, which determines whether the state of a qubit or an entangled resource across quantum repeaters, such as a Bell pair, is defective or not.

For each step in the circuit, only one operation is assumed to be performable to the same qubit. Consequentially, for two different controlled gates with two different target qubits, if they share the same control qubit, a total of 2 depth at minimum is required to finish both operations. Also, the physical distance between each node is not taken into consideration in the simulation. Thus, each node is assumed to be capable of perfectly delivering the classical feedforward message to the destination node within one circuit depth.

In this thesis, for simplicity, the term *input fidelity* refers to initial resource fidelity and *output fidelity* refers to the joint fidelity of the resulting two crossing-over entangled pairs at the end of each protocol.

Here, fidelity $F = 1 - p = \langle \psi | \rho | \psi \rangle$, where p is the error rate and $|\psi\rangle$ is the ideal pure state. As explained in section 2.12, errors propagate through circuits. The output fidelity is calculated by $F_{\text{output}} = 1 - p'$, where p' is the probability of at least one error present on either entangled output at the end of the protocol. For each datapoint of short quantum circuit simulations, section 6.3.1 and 6.3.2, the simulation either stops if 100 thousand residual errors have been accumulated or if 100 million trials have been performed. For section 6.3.3, due to computation power restrictions, a maximum of 20 thousand residual errors have been accumulated or 1 million trials have been performed.

6.3 Simulation results and evaluation

6.3.1 Initial resource generation

Before moving on to the full circuit evaluation, we first focus on a simpler circuit that consists of two qubits aimed for generating an initial resource. In QNC and ES, quantum repeaters are assumed to be sharing Bell pairs ($\frac{1}{\sqrt{2}}(|00\rangle + |11\rangle)$) as communication resources. On the other hand, MQNC requires cluster states ($\frac{1}{\sqrt{2}}(|0+\rangle + |1-\rangle)$) to be shared as the protocol works based on measurement-based quantum computing. As mentioned before in section 5.1.1, circuits for generating a 2-qubit cluster state and a Bell pair can be implemented in a similar way using a CNOT gate, but it is more natural to assume that the 2-qubit cluster state generation is done through a CZ gate operation as it is more efficient in terms of the circuit depth. For convenience, each quantum circuit is reintroduced in Figure 6.1.

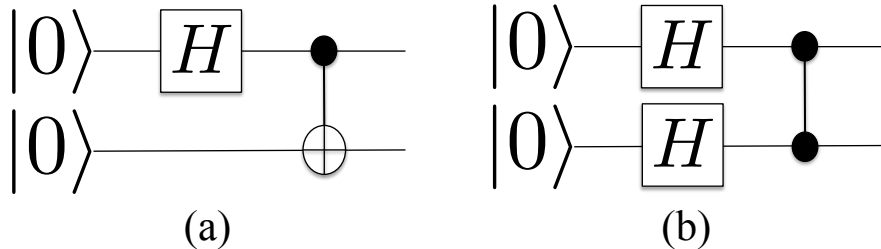


Figure 6.1: Quantum circuit for generating initial resources (a) Quantum circuit for Bell pair generation (b) Quantum circuit for 2 qubit cluster state generation

Errors on initial resources

Qubits are commonly prepared with the state $|0\rangle$ before starting the actual computation. The state $|0\rangle$ is not in a superposition state, and is therefore measurable with respect to the Z-basis without disturbing the state. If the measurement result of an initialized qubit turns out to be $|1\rangle$ instead of $|0\rangle$, one can simply apply an X gate operation to flip the quantum state to $|0\rangle$. However, in some cases, a qubit might not be prepared in the desired state due to an erroneous measurement or an erroneous X gate operation - giving $|1\rangle$ due to a bit-flip (X) error on the qubit. For simplicity, the phase error is assumed to be nonexistent.

Error type	Probability
$I 0\rangle$	$1 - p$
$X 0\rangle$	p

The first simulation studies the impact of initial qubit resource fidelity on the output fidelity for circuits introduced in Figure 6.1. For this particular problem set, the relation between the input fidelity and the output fidelity can be analytically calculated. For a Bell pair generation, the qubit state branches into 4 patterns with or without errors, which includes I_0I_1 , I_0X_1 , X_0I_1 and X_0X_1 . For details regarding the relation between the input state and the output state, see Table 6.3 and Table 6.4. The stabilizers of a Bell pair are X_0X_1 and Z_0Z_1 , and X_0Z_1 and Z_0X_1 stabilize a 2-qubit cluster state.

Table 6.3: Bell pair circuit error propagation of input error and the correlated output state. $|\psi_{init}\rangle = |0_20_1\rangle$ and $|\psi_{out}\rangle = \frac{1}{\sqrt{2}}(|00\rangle + |11\rangle)$

Input state	Output state	Error
$I_0I_1 \psi_{init}\rangle$	$I_0I_1 \psi_{out}\rangle$	No
$I_0X_1 \psi_{init}\rangle$	$I_0X_1 \psi_{out}\rangle$	Yes
$X_0I_1 \psi_{init}\rangle$	$Z_0I_1 \psi_{out}\rangle$	Yes
$X_0X_1 \psi_{init}\rangle$	$Z_0X_1 \psi_{out}\rangle$	Yes

Table 6.4: Cluster state circuit error propagation of input error and the correlated output state. $|\psi_{init}\rangle = |0_2 0_1\rangle$ and $|\psi_{out}\rangle = \frac{1}{2}(|00\rangle + |01\rangle + |10\rangle - |11\rangle)$

Input state	Output state	Error
$I_0 I_1 \psi_{init}\rangle$	$I_0 I_1 \psi_{out}\rangle$	No
$I_0 X_1 \psi_{init}\rangle$	$I_0 Z_1 \psi_{out}\rangle$	Yes
$X_0 I_1 \psi_{init}\rangle$	$Z_0 I_1 \psi_{out}\rangle$	Yes
$X_0 X_1 \psi_{init}\rangle$	$Z_0 Z_1 \psi_{out}\rangle$	Yes

For both circuits, only 1 pattern out of 4 outputs a noiseless entangled pair. It is not too hard to find out that with an average of 50% of input fidelity, the output fidelity is $0.5^2 = 0.25\%$, as the probability of both having no error (II) is the joint fidelity of both qubits. To generalize, with the input fidelity of F , the output fidelity is F^2 . The analytical result agreed with the simulated results. All results are shown below at Figure 6.2.

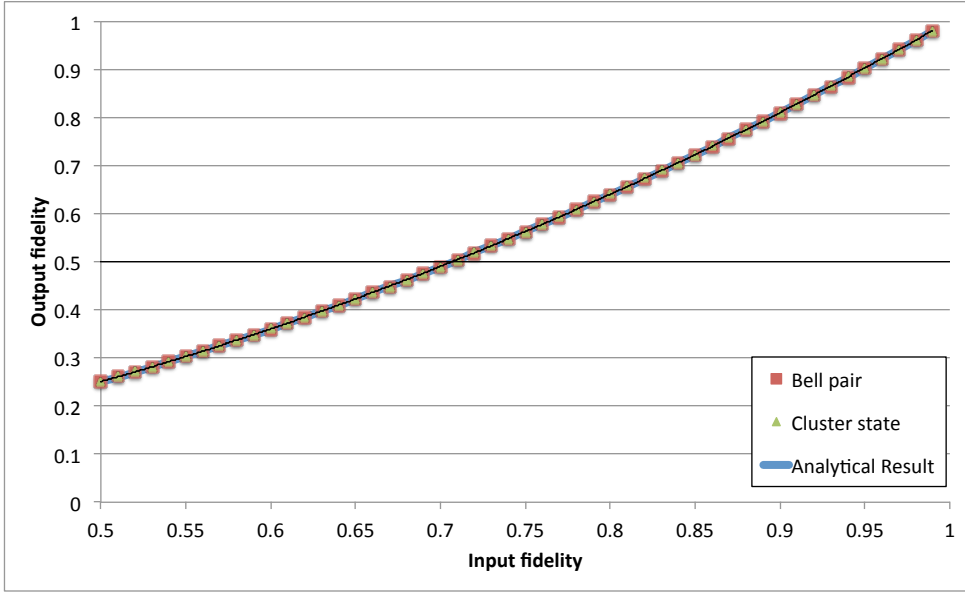


Figure 6.2: Impact of input fidelity to output fidelity in initial shared resource generation

As discussed, both circuits share the same error tolerance against initial resources. However, considering the difference in controlled operations and the extra single-qubit gate that is required for the cluster state generation, the physical cost of each method is still questionable but cannot be discussed in the simulation. In order to obtain a minimum fidelity of 50%, the input fidelity must be greater than 71%.

Fixed initial resource fidelity and variable error rate on local operation

Next, we hold the input qubit fidelity at $F_{input} = 0.98$, and vary the local operation accuracy from $F_{operation} = 50\%$ to $F_{operation} = 99\%$ using $\Delta F_{operation} = 1\%$. Here, the

term local operation refers to qubit memories and gate operations. Each error, X, Y and Z, share the same weighted probability. Possible error patterns for a single-qubit operation and a two-qubit operation are listed below in Table 6.5.

Table 6.5: Possible types of errors caused by gate operations. (a) Error model of single-qubit gates where $|\psi_0\rangle$ is a quantum state and p = gate error rate. (b) Error model of two-qubit gates where $|\psi_{0,1}\rangle$ is a composite quantum state and p = gate error rate.

(a) Single-qubit gate		(b) Two-qubit gate	
Error type	Probability	Error type	Probability
$I \psi_0\rangle$	$1 - p$	$I_0 I_1 \psi_{0,1}\rangle$	$1 - p$
$X \psi_0\rangle$	$p/3$	$I_0 X_1 \psi_{0,1}\rangle$	$p/15$
$Y \psi_0\rangle$	$p/3$	$I_0 Y_1 \psi_{0,1}\rangle$	$p/15$
$Z \psi_0\rangle$	$p/3$	$I_0 Z_1 \psi_{0,1}\rangle$	$p/15$
		$X_0 I_1 \psi_{0,1}\rangle$	$p/15$
		$X_0 X_1 \psi_{0,1}\rangle$	$p/15$
		$X_0 Y_1 \psi_{0,1}\rangle$	$p/15$
		$X_0 Z_1 \psi_{0,1}\rangle$	$p/15$
		$Y_0 I_1 \psi_{0,1}\rangle$	$p/15$
		$Y_0 X_1 \psi_{0,1}\rangle$	$p/15$
		$Y_0 Y_1 \psi_{0,1}\rangle$	$p/15$
		$Y_0 Z_1 \psi_{0,1}\rangle$	$p/15$
		$Z_0 I_1 \psi_{0,1}\rangle$	$p/15$
		$Z_0 X_1 \psi_{0,1}\rangle$	$p/15$
		$Z_0 Y_1 \psi_{0,1}\rangle$	$p/15$
		$Z_0 Z_1 \psi_{0,1}\rangle$	$p/15$

As shown, after a single-qubit operation, the output branches into 4 different states. Similarly, there are 16 different possible output states after a two-qubit operation. The simulation results are shown in Figure 6.3.

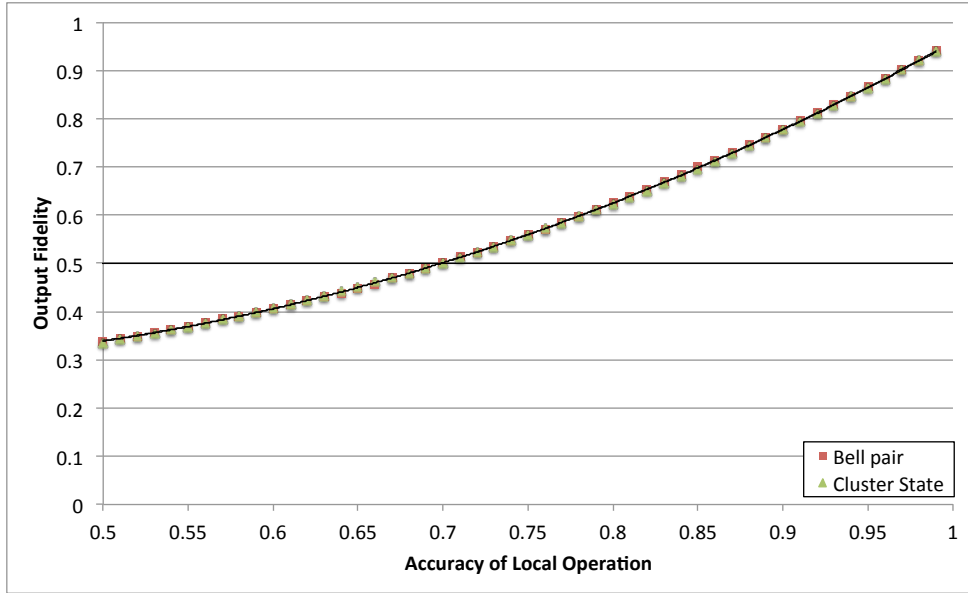


Figure 6.3: Impact of local operation accuracy to output fidelity in initial shared resource generation. Input fidelity is fixed to $F_{input} = 0.98\%$.

The Bell pair circuit and the 2-qubit cluster state circuit have the error tolerance. In order to acquire a minimum fidelity of $F_{output} = 50\%$, both resource generation requires at least 70% local gate accuracy.

6.3.2 Linear 3-qubit entanglement generation

Next, two quantum circuits that operates on 3 qubits as in Figure 6.4 are introduced. Each circuit consumes two initialized entangled states and creates a linearly entangled 3-qubit entangled state - 1 qubit is measured in the process of encoding. Subscripts of gates denote the operation identifier, which is there to help readers identify which measurement is connected to which byproduct operation.

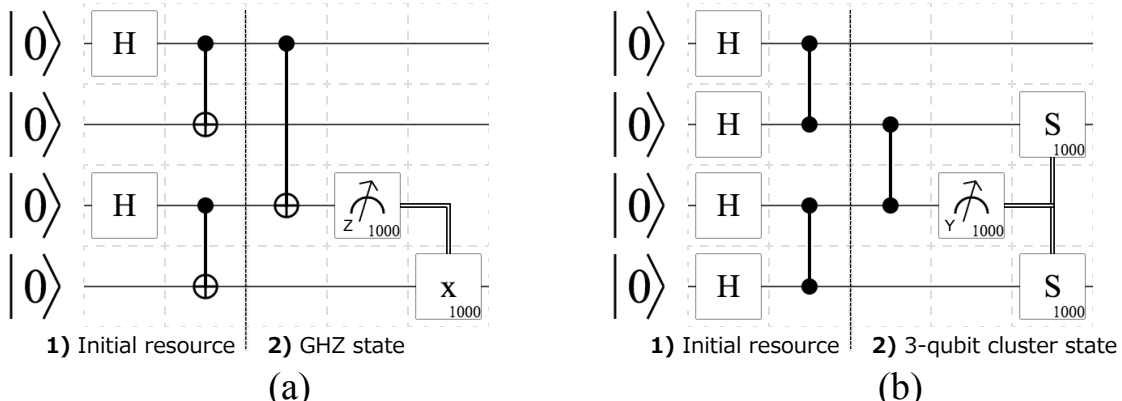


Figure 6.4: Quantum circuit for generating linear 3-qubit entanglement (a) Quantum circuit for GHZ state generation (b) Quantum circuit for 3 qubit cluster state generation.

Errors on initial resources

In real networking, entangled pairs are repeatedly generated between quantum repeaters [40]. Therefore, from this section, shared resources are assumed to be prepared beforehand independent from the protocol. The first two columns of the circuits are excluded from the simulation and the term *input fidelity* is redefined to the average fidelity of the previously shared initial resources. The types of errors that may be present on each resource is summarized in Table 6.6 - some errors do not appear because they stabilize the state.

Table 6.6: Possible types of errors on initial resources. (a) Error model of Bell pairs where $|\psi_{0,1}\rangle$ is a Bell pair and p = initial resource error rate. (b) Error model of cluster states where $|\psi_{0,1}\rangle$ is a cluster state and p = initial resource error rate.

(a) Bell pair		(b) Cluster state	
Error type	Probability	Error type	Probability
$I_0I_1 \psi_{0,1}\rangle$	$1 - p$	$I_0I_1 \psi_{0,1}\rangle$	$1 - p$
$I_0X_1 \psi_{0,1}\rangle$	$p/12$	$I_0X_1 \psi_{0,1}\rangle$	$p/12$
$I_0Y_1 \psi_{0,1}\rangle$	$p/12$	$I_0Y_1 \psi_{0,1}\rangle$	$p/12$
$I_0Z_1 \psi_{0,1}\rangle$	$p/12$	$I_0Z_1 \psi_{0,1}\rangle$	$p/12$
$X_0I_1 \psi_{0,1}\rangle$	$p/12$	$X_0I_1 \psi_{0,1}\rangle$	$p/12$
$X_0X_1 \psi_{0,1}\rangle$	0	$X_0X_1 \psi_{0,1}\rangle$	$p/12$
$X_0Y_1 \psi_{0,1}\rangle$	$p/12$	$X_0Y_1 \psi_{0,1}\rangle$	$p/12$
$X_0Z_1 \psi_{0,1}\rangle$	$p/12$	$X_0Z_1 \psi_{0,1}\rangle$	0
$Y_0I_1 \psi_{0,1}\rangle$	$p/12$	$Y_0I_1 \psi_{0,1}\rangle$	$p/12$
$Y_0X_1 \psi_{0,1}\rangle$	$p/12$	$Y_0X_1 \psi_{0,1}\rangle$	$p/12$
$Y_0Y_1 \psi_{0,1}\rangle$	0	$Y_0Y_1 \psi_{0,1}\rangle$	0
$Y_0Z_1 \psi_{0,1}\rangle$	$p/12$	$Y_0Z_1 \psi_{0,1}\rangle$	$p/12$
$Z_0I_1 \psi_{0,1}\rangle$	$p/12$	$Z_0I_1 \psi_{0,1}\rangle$	$p/12$
$Z_0X_1 \psi_{0,1}\rangle$	$p/12$	$Z_0X_1 \psi_{0,1}\rangle$	0
$Z_0Y_1 \psi_{0,1}\rangle$	$p/12$	$Z_0Y_1 \psi_{0,1}\rangle$	$p/12$
$Z_0Z_1 \psi_{0,1}\rangle$	0	$Z_0Z_1 \psi_{0,1}\rangle$	$p/12$

The simulation result for assessing the impact of input fidelity on the output fidelity is shown in Figure 6.5. The cluster state circuit starts off with better input error tolerance, however, the difference becomes indistinguishable as input fidelity gets higher. The difference in output fidelity gets less than 1% if $F_{input} \geq 73\%$. To retain a minimum output fidelity of $F_{output} = 50\%$, GHZ circuit requires a fidelity of $F_{input} \geq 71\%$ and $F_{input} \geq 70\%$ for cluster state circuit.

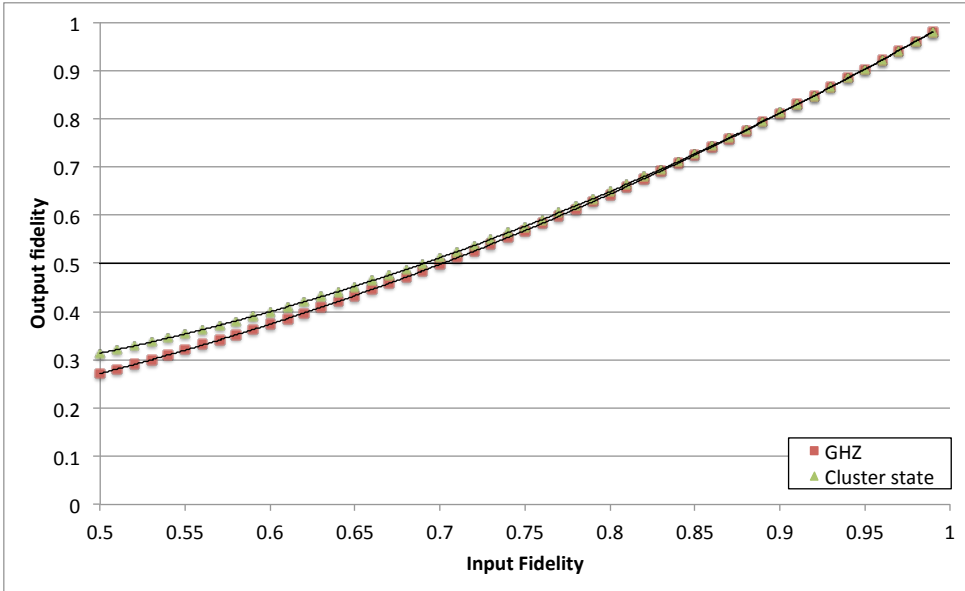


Figure 6.5: Impact of input fidelity on output fidelity in linear 3-qubit entanglement generation

Fixed initial resource fidelity and variable error rate on local operation

Shared resources across quantum repeaters are commonly purified periodically to improve its fidelity. Therefore, it is more likely to consider that those shared resources have high enough fidelities. The input fidelity is held as a constant $F_{input} = 98\%$ and local gate accuracy is changed from $F_{operation} = 50\%$ to $F_{operation} = 100\%$ using $\Delta F_{operation} = 1\%$. The simulation result with this settings is shown in Figure 6.6. Both circuits' output fidelity becomes greater than 50% when $F_{operation} \geq 93\%$. From that point, cluster state generation has slightly better error tolerance than GHZ generation by approximately 0.7% when $F_{operation} = 100\%$.

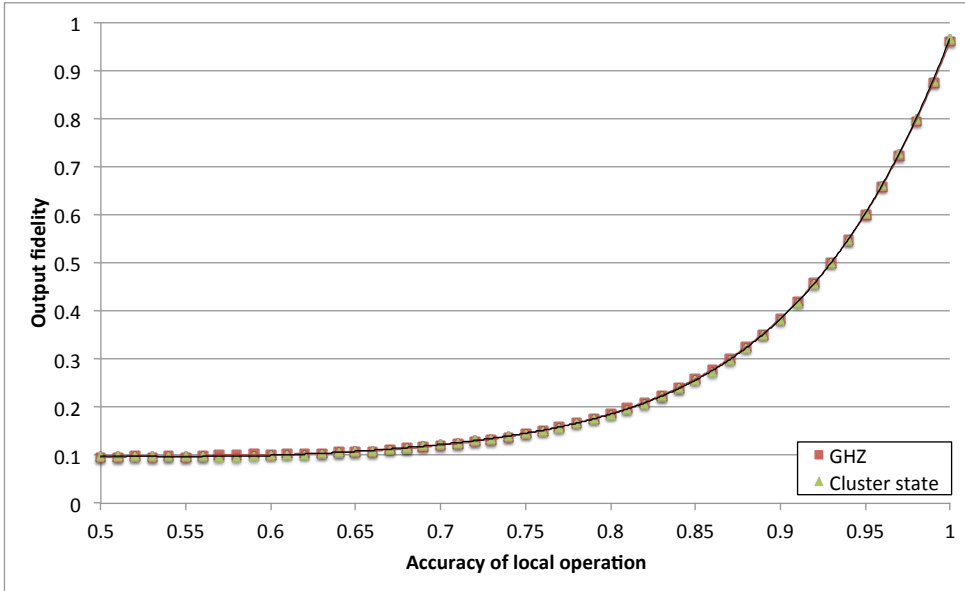


Figure 6.6: Impact of local gate accuracy on output fidelity in linear 3-qubit entanglement generation. Input fidelity is fixed to $F_{input} = 0.98\%$.

6.3.3 Full MQNC circuit

As mentioned at the begining of the chapter, alternative methods are evaluated using the same procedure and compared statistically in order to assess the performance of the proposed protocol. The first alternative method is the prior quantum network coding (QNC) technique introduced as in Related work in section 4. To be clear, QNC does not use MBQC to complete the network coding task but instead uses CNOT gate operations and measurements to imitate the procedure of the classical network coding by creating parities in stead of XOR operations. Operations required for this protocol needs to be applied one by one going through the proper procedure, which creates a significant amount of dependencies between qubit operations. The quantum circuit for QNC is shown below at Figure 6.7(a).

Buffer-space multiplexing using entanglement swapping (ES) is not related to network coding but is one of the easiest ways to resolve the bottleneck problem. This thesis will consider the simplest encoding procedure of entanglement swapping in order to make the comparison consistent over results in related work. The details of the quantum circuit for ES can be seen in Figure 6.7(b).

Compared to QNC, MQNC does not follow the traditional network coding procedure, but focuses on creating two crossing-over cluster states topologically by exploiting MBQC. The evaluated quantum circuit for MQNC is shown below at Figure 6.7(c).

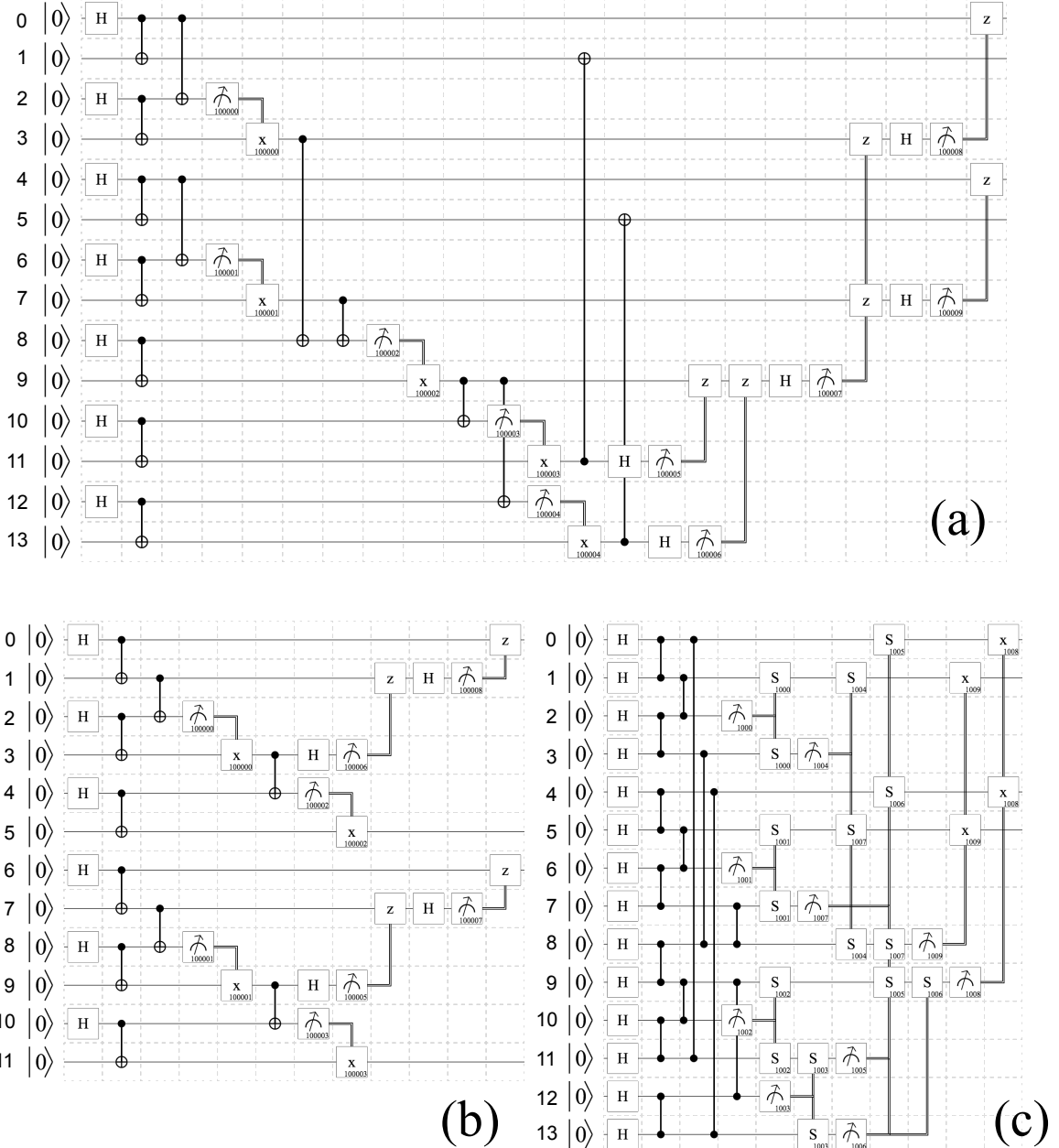


Figure 6.7: Evaluated quantum circuits. (a) Quantum circuit for Quantum Network Coding over Repeater Networks. (b) Quantum circuit for Buffer-space Multiplexing using Entanglement Swapping. (c) Quantum circuit for Measurement Based Quantum Network Coding over Repeater Networks.

Among all protocols, MQNC has the shortest circuit depth. Other statistical characteristics of each protocol are summarized in Table 6.8.

Errors on initial resources

Before simulating the entire circuit with all error sources affecting the result, we first simulate the propagation of errors present in the initial resources but without local gate

Table 6.7: Characteristics of Protocols

	MQNC	QNC	ES
Number of qubits	14	14	12
Number of entangling operations	7	7	6
Number of single-qubit gates (byproduct operators)	20(20)	16(11)	12(8)
Number of two-qubit gates	8	8	4
Number of measurements	10	10	4
Circuit depth	11	23	12
KQ (Circuit depth \times number of qubits)	154	322	144

errors in order to assess the tolerance and efficacy of initial fidelity to output fidelity in all three protocols. In this section, three scenarios have been simulated by changing the input fidelity from $F_{input} = 50\%$ to $F_{input} = 99\%$ using $\Delta F_{input} = 1\%$.

The first scenario is the Z errors present on the initially shared entangled pairs of qubits. For simplicity, errors are assumed to only exist on the qubits that are labeled with odd numbers, after the initialization, as in Figure 6.7. As an example, the initial entangled resource of qubit 0 and qubit 1 may have a state of $(I_0 \oplus Z_1) |\psi_{0,1}\rangle$ with probability $P_{error} = p$, or $(I_0 \oplus I_1) |\psi_{0,1}\rangle$ with probability $P_{clean} = 1 - p$. The simulation result is shown below at Figure 6.8.

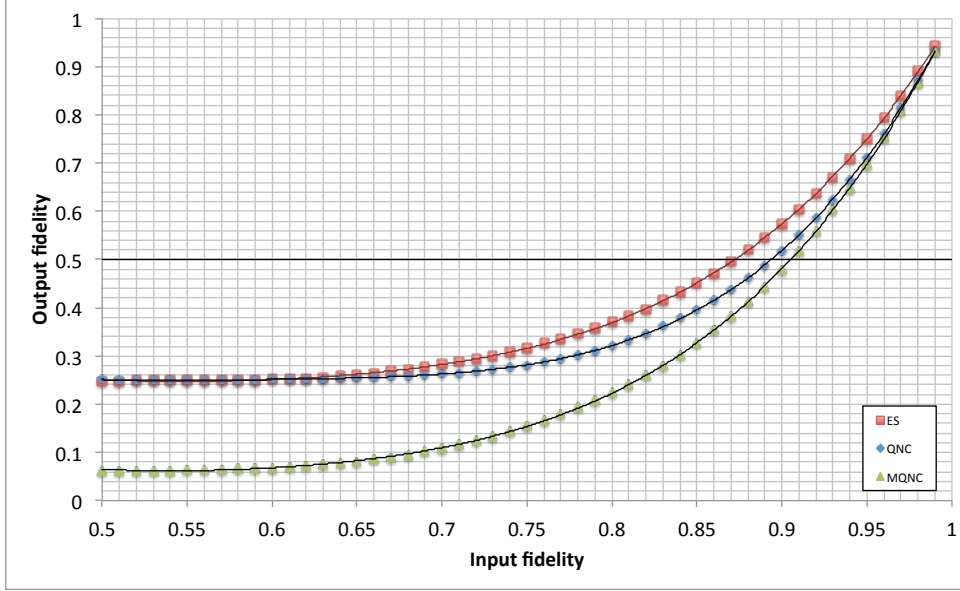


Figure 6.8: Impact of input fidelity on output fidelity in three protocols. Probabilistic Z error on qubits labeled with odd numbers.

Overall, ES has the highest initial resource Z error tolerance among the protocols. Although ES and QNC have similar results with lower fidelity, the difference in ES and QNC output fidelity $|F_{output}^{qnc} - F_{output}^{es}| \leq 1\%$ when $F_{input} \leq 33\%$. On the other

hand, MQNC starts with the lowest output fidelity but shares the same behavior as QNC with higher fidelity. The main reason for this is because the Z error on a Bell pair $|\Phi^+\rangle$ only changes its state to $|\Phi^-\rangle$, which are two patterns in total. With a 50% chance of having a Z error on Bell pair, the joint fidelity drops to $1/2^2 = 25\%$. On the other hand, a Z error on a 2-qubit cluster state stochastically changes the state to $\frac{1}{2} |00\rangle + |01\rangle - |10\rangle + |11\rangle$ with a ZI error, $\frac{1}{2} |00\rangle - |01\rangle + |10\rangle + |11\rangle$ with a IZ error, and $\frac{1}{2} |00\rangle - |01\rangle - |10\rangle + |11\rangle$ with a ZZ error. That is a total of 4 patterns, which the joint fidelity drops to $1/4^2 = 6.25\%$. The difference in MQNC and QNC output fidelity $|F_{output}^{mqnc} - F_{output}^{qnc}| \leq 1\%$ when $F_{input} \geq 96\%$.

The second scenario is similar to the first scenario but with X errors present on the initially shared entangled pairs of qubits labeled with odd numbers. The simulation result is shown in Figure 6.9.

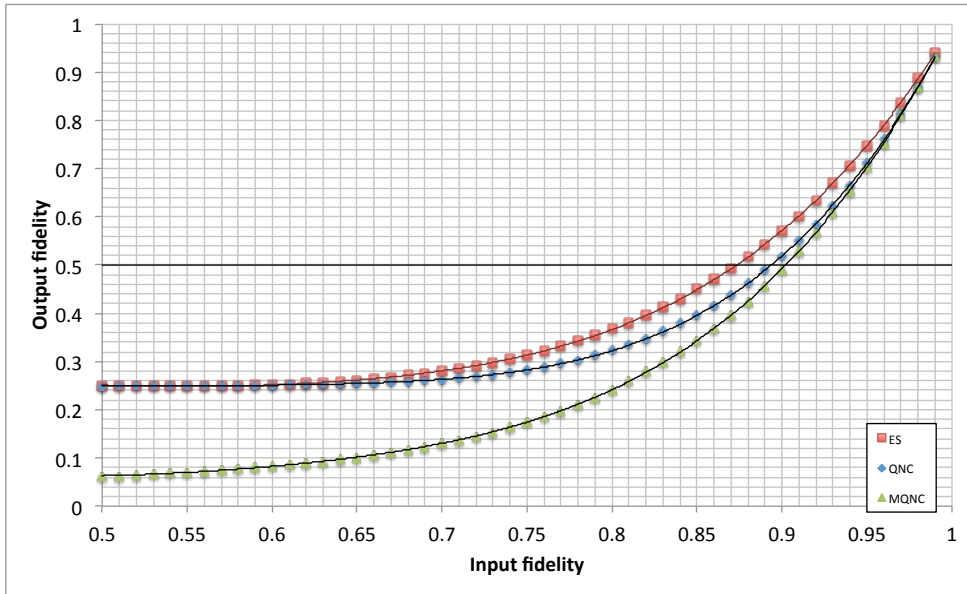


Figure 6.9: Impact of input fidelity on output fidelity in three protocols. Probabilistic X error on qubits labeled with odd numbers.

The error tolerance for QNC and ES does not change for Z errors and X errors. To the contrary, MQNC has slightly better error tolerance to X errors than Z errors. Similar to the case with only Z error, the Z error changes the Bell pair state $|\Phi^+\rangle$ to $|\Psi^+\rangle$, which has only 2 patterns. Therefore, with a 50% probability of X error on each Bell pair, both of them combined results in a joint fidelity of $1/(2^2) = 25\%$. To the contrary, the 2-qubit cluster state have 4 patterns with or without X errors - $\frac{1}{2} |00\rangle + |01\rangle + |10\rangle - |11\rangle$, $\frac{1}{2} |10\rangle + |11\rangle + |00\rangle - |01\rangle$, $\frac{1}{2} |00\rangle + |01\rangle - |10\rangle + |11\rangle$ and $\frac{1}{2} |10\rangle + |11\rangle - |00\rangle + |01\rangle$. Therefore, with a 50% error rate, the joint fidelity drops to $1/4^2 = 6.25\%$. The difference in MQNC and QNC output fidelity $|F_{output}^{mqnc} - F_{output}^{qnc}| \leq 1\%$ when $F_{input} \geq 95\%$.

In the last scenario, not only Z or X errors but any other errors can exist on any initial resources. Errors on entangled resources have the same weighted probability (for details, refer to Table 6.6).

As shown in Figure 6.10, MQNC and ES have similar initial error tolerance, and QNC is slightly left behind. In order to retain an output fidelity of $F_{output} = 50\%$, QNC and MQNC require an input fidelity of at least $F_{input} = 89\%$, while QNC requires an extra 2% in order to achieve the same goal.

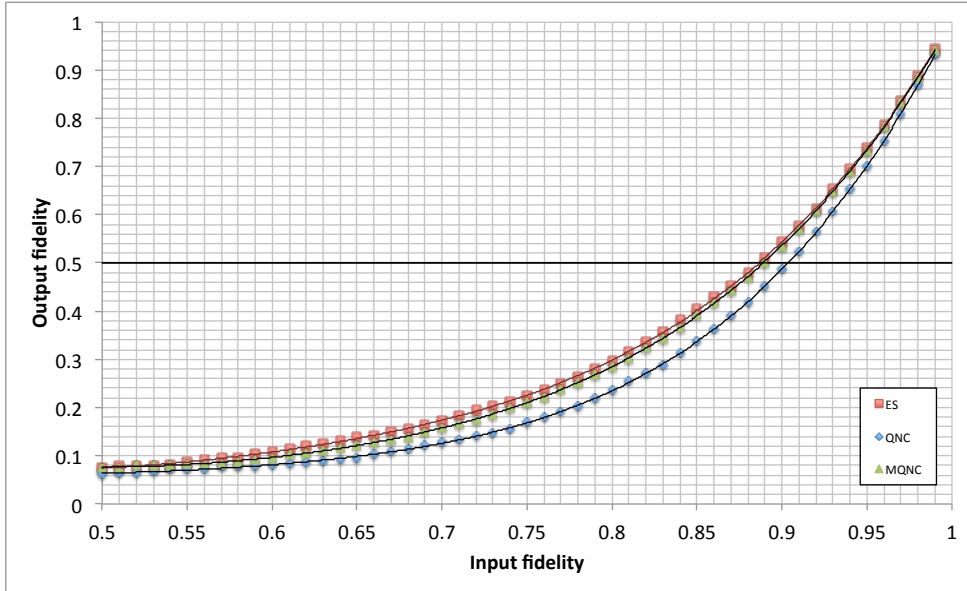


Figure 6.10: Impact of input fidelity on output fidelity in three protocols. Probabilistic errors on all qubits.

Fixed initial resource fidelity and variable error rate on local operation

Finally, all error sources, such as qubit memories and measurements, are assumed to be actively generating errors. A single-qubit operation may emit one error out of 3 possibilities, X, Y and Z error, with equal probability. Similarly, after a two-qubit operation, there is no error, or at least one X, Y or Z error is present on either qubit. Initial fidelity is fixed to $F_{input} = 98\%$ and other error rates are changed concurrently from $F_{operation} = 98\%$ to $F_{operation} = 100\%$ with $\Delta F_{operation} = 0.05\%$. The simulation result is shown in Figure 6.11.

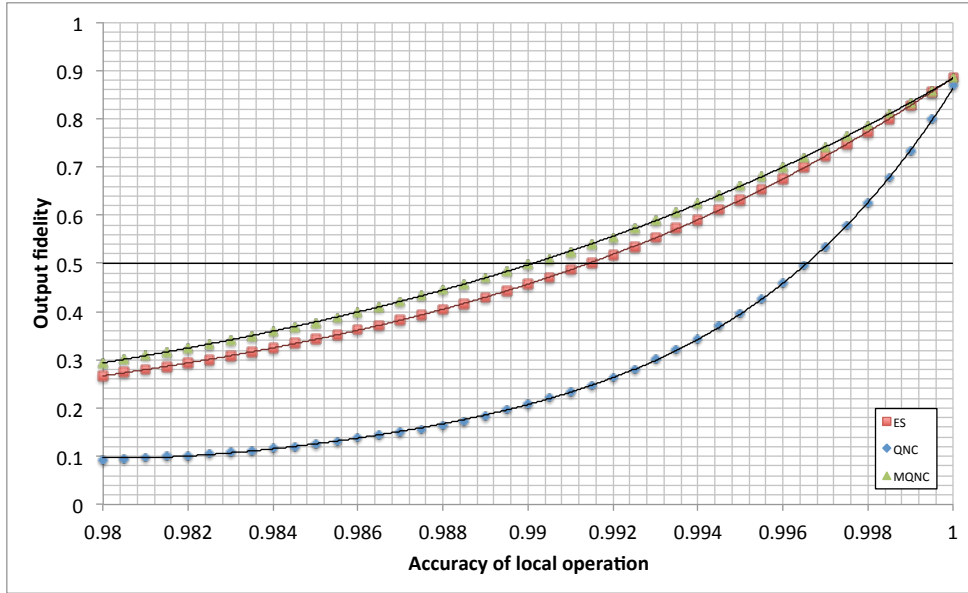


Figure 6.11: Impact of local operation accuracy to output fidelity in three protocols. Input fidelity is fixed to $F_{input} = 98\%$.

The average output fidelity is calculated by:

$$\text{Average output fidelity} = \frac{\sum_{i=0}^{n-1} (f(0.98 + i\Delta x))}{n} \quad (6.1)$$

where $f(x)$ is the function representing the correlation between the local operation accuracy and the output fidelity in each protocol, Δx is the interval of data points $\Delta x = 0.0005$ and n is the number of data points $n = 41$.

In order to find the approximate area under each curve, Average Riemann Sum has been used:

$$\text{Average Riemann Sum} = \Delta x * \sum_{i=1}^n \left(\frac{f(0.98 + i\Delta x) + f(0.98 + (i-1)\Delta x)}{2} \right) \quad (6.2)$$

The average slope is calculated by:

$$\text{Average slope} = \frac{\sum_{i=1}^n \frac{f(0.98+i\Delta x) - f(0.98+(i-1)\Delta x)}{\Delta x}}{n} \quad (6.3)$$

Table 6.8: Characteristics of Protocols

	MQNC	QNC	ES
Average output fidelity	0.52896	0.29273	0.49880
Maximum output fidelity	0.88481	0.86767	0.88668
Minimum output fidelity	0.29334	0.09314	0.26683
Total area (Average Riemann Sum)	0.01055	0.00576	0.00994
Average slope	29.57325	38.72645	30.99265
Maximum slope	51.70000	138.15600	61.434
Minimum slope	14.00600	0.83400	12.49600

As shown, with the simulation model of all error sources, MQNC has the highest output fidelity yet the gentlest slope in average. Although the maximum output fidelity of each protocol converges to a similar point, the area under the curve of MQNC and QNC is approximately twice of QNC's, which also means that MQNC and QNC tolerates about twice the local error rate of QNC. Moreover, QNC has the lowest and highest rate of change, which indicates that the output fidelity of QNC significantly depends on the local error rate.

As each protocol has its own circuit characteristics, the errors that appear on the entangled output differs. The details of the error distribution on entangled outputs for each protocol when $F_{input} = 98\%$ and $F_{operation} = 98\%$ is shown in Figure 6.12. Percentage differences of error types for each protocol are summarized in Table 6.9, Table 6.10, and Table 6.11 accordingly. Errors such as I_0X_1 and X_0I_1 are physically indistinguishable, therefore, the X-axis and Y-axis for each distribution graph is invertible. Percentage difference is calculated by:

$$\text{Percentage difference} = \frac{|\text{Error Rate}_{output1} - \text{Error Rate}_{output2}|}{\frac{\text{Error Rate}_{output1} + \text{Error Rate}_{output2}}{2}} \times 100 \quad (6.4)$$

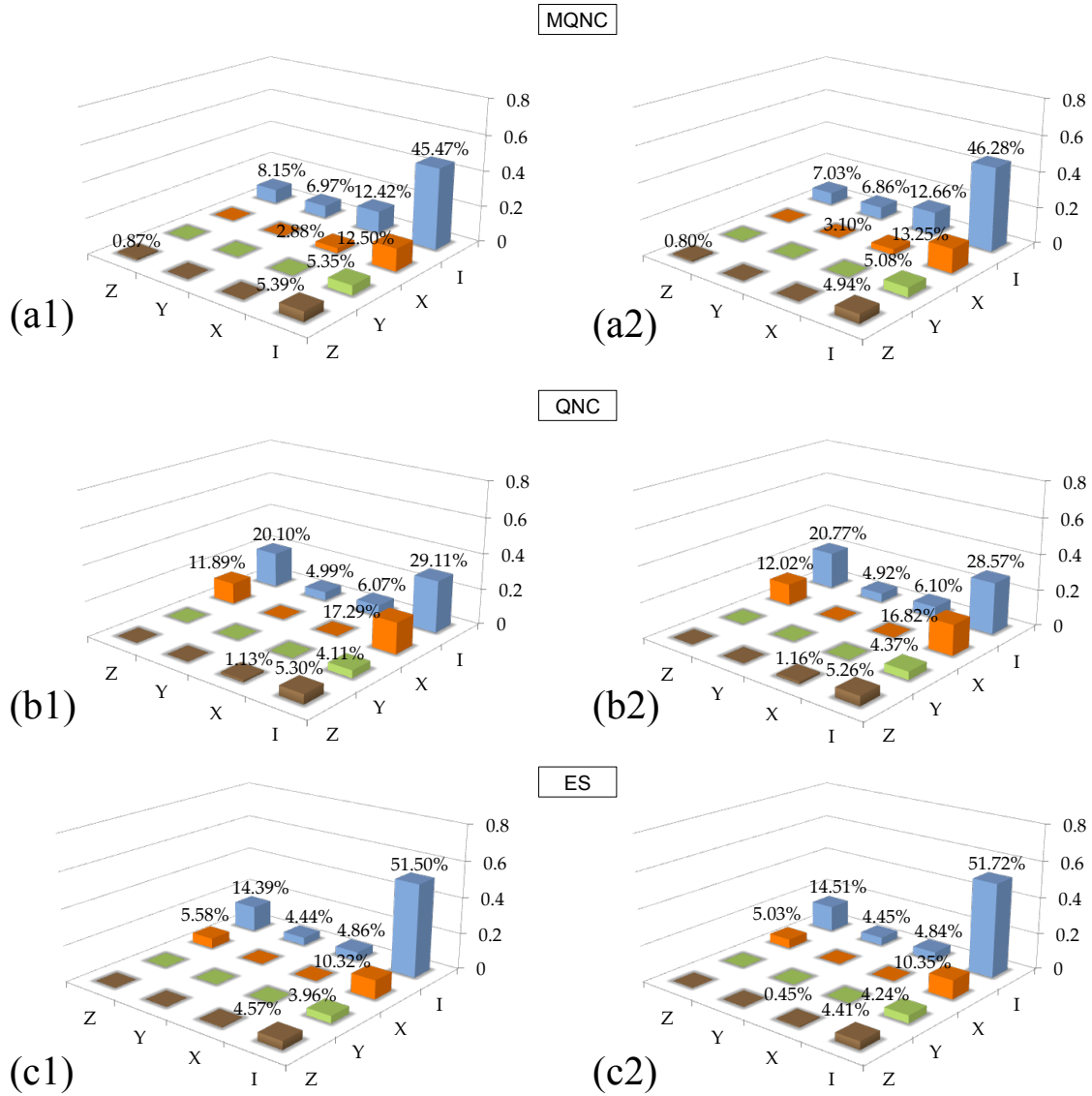


Figure 6.12: Error distribution of one entangled outputs. (a1) Error distribution of cluster state formed by qubit 1 and qubit 6 in MQNC. (a2) Error distribution of cluster state formed by qubit 2 and qubit 5 in MQNC. (b1) Error distribution of Bell pair formed by qubit 1 and qubit 6 in QNC. (b2) Error distribution of Bell pair formed by qubit 2 and qubit 5 in QNC. (c1) Error distribution of Bell pair formed by qubit 1 and qubit 6 in ES. (c2) Error distribution of Bell pair formed by qubit 7 and qubit 12 in ES. Distribution at input fidelity $F_{input} = 98\%$ and local operation accuracy $F_{operation} = 98\%$.

Table 6.9: Percentage difference of error distributions in MQNC

	I	X	Y	Z
I	1.7632%	5.8223%	5.1735%	8.7474%
X	1.9754%	7.1141%	-	-
Y	1.4899%	-	-	-
Z	14.7581%	-	-	8.9239%

Table 6.10: Percentage difference of error distributions in ES

	I	X	Y	Z
I	0.4133%	0.4139%	0.1693%	0.8165%
X	0.2670%	-	-	10.2625%
Y	6.9219%	-	-	-
Z	3.5205%	17.7370%	-	-

Table 6.11: Percentage difference of error distributions in QNC

	I	X	Y	Z
I	1.8680%	0.5139%	1.2623%	3.2999%
X	2.7710%	-	-	1.0754%
Y	5.9812%	-	-	-
Z	0.7895%	2.4242%	-	-

The highest percentage difference obtained is 17.7% in ES, however, the error distribution is mostly symmetrical over 2 outputs for all protocols. Most interestingly, the output joint fidelity of MQNC when $F_{input} = 98\%$ and $F_{operation} = 98\%$ is higher than that of ES, even though entangled outputs of ES separately retain higher output fidelity. As a hypothesis, this is caused by the two byproduct operators for each measurement in MQNC, which synchronizes propagation of errors throughout the circuit - multiple errors occur or cancel out simultaneously.

The change in error distribution over the change in local operation accuracy is plotted in Figure 6.13.

H

Table 6.12: Slope change of error rate by type. This reflects the sensitivity to each type of error.

	IX	IY	IZ	XI	XX	YI	ZI	ZZ
Ave. slope	-507.31	-234.57	-192.69	-519.74	-125.90	-308.26	-330.32	-41.54
Max. slope	996.03	487.98	301.90	936.68	248.39	637.15	599.52	110.54
Min. slope	103.08	20.96	7.35	102.88	11.96	20.42	114.18	3.39

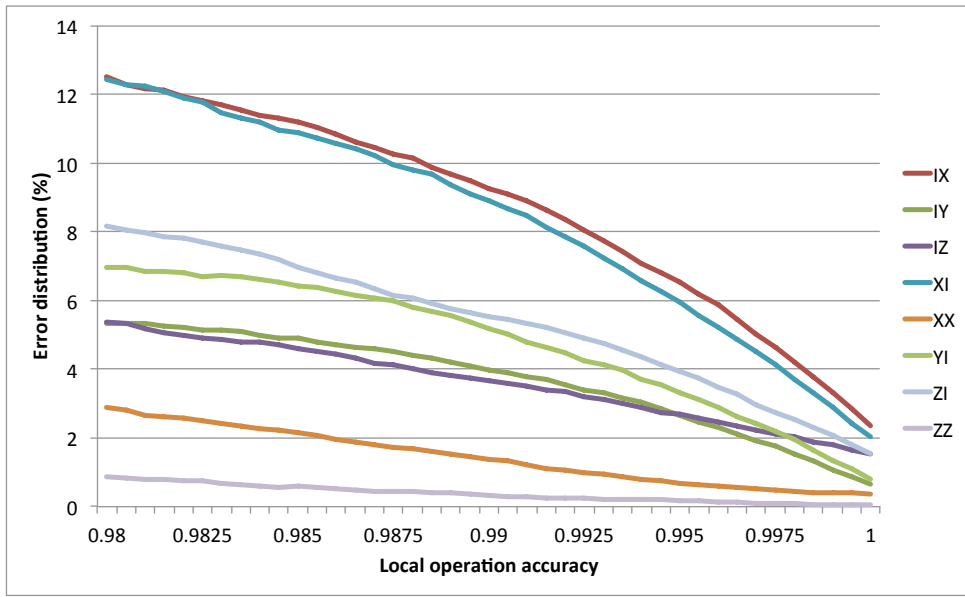


Figure 6.13: Error distribution versus local operation accuracy in MQNC. Input fidelity is fixed to $F_{input} = 98\%$.

As seen, MQNC mostly suffers from IX and XI error in all situations - a bit-flip error on either qubit. As a matter of fact, those errors combined covers approximated one fourth of the total probability. On the other side, with a fixed initial resource error of $F_{input} = 98\%$, the probability of ZZ and XX error drops gradually to $P(ZZ) \approx 0.04\%$ and $P(XX) \approx 0.36\%$ as local operation accuracy approaches to 1. As those error rate converges to a certain point, not much benefit can be obtained from further improvement of local operation accuracy, when the local operation accuracy is high enough. The error rate for ZZ error drops by 0.002% by an improvement of local operation accuracy $F_{operation} = 99.995\%$ to $F_{operation} = 100\%$. While the slope of ZZ error and XX error gets flatter, other error types' probabilities drop more aggressively as the local operation accuracy approaches to 1. As a matter of fact, IX error rate decreases by 0.5% when local operation accuracy is improved from $F_{operation} = 99.995\%$ to $F_{operation} = 100\%$.

Fixed initial resource fidelity, perfect memory and erroneous local operation

Lastly, qubit memories are assumed to be ideal, and therefore, qubits that are waiting for other process do not get affected by noise. Other error variables including gates

and measurements stay as the independent variable with a domain of $F_{operation} = 98\%$ to $F_{operation} = 100\%$ with a constant initial resource fidelity of $F_{input} = 98\%$. The simulation results are shown in Figure 6.14 with a summarized statistics in Table 6.13.

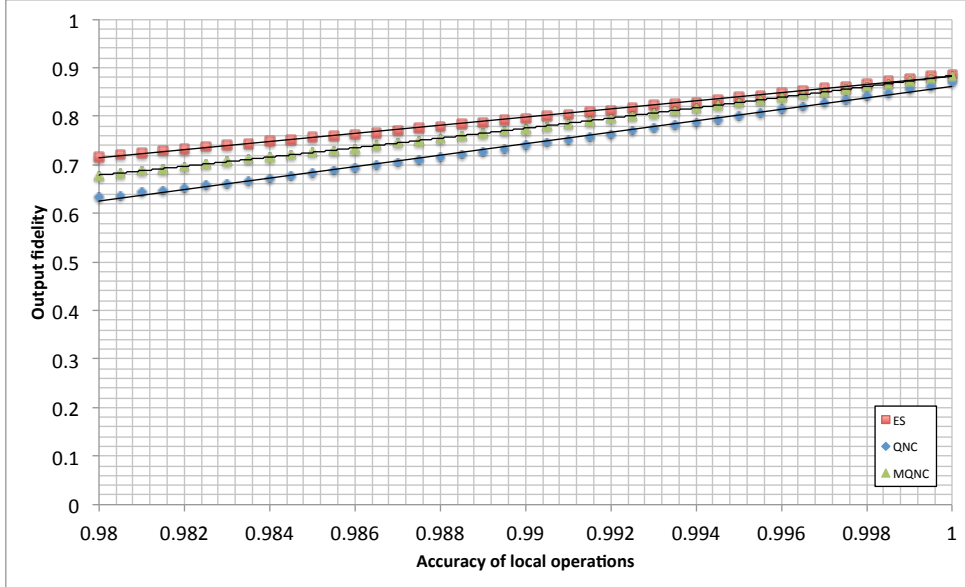


Figure 6.14: Impact of local operation accuracy to output fidelity in three protocols. Memory error rate is fixed to $F_{memory} = 100\%$. Input fidelity is fixed to $F_{input} = 98\%$.

Table 6.13: Characteristics of Protocols with perfect memory

	MQNC	QNC	ES
Average output fidelity	0.77744	0.74353	0.79843
Maximum output fidelity	0.88347	0.87000	0.88695
Minimum output fidelity	0.67892	0.63391	0.71714
Total area (Average Riemann Sum)	0.00039	0.00037	0.00040
Average slope	10.22735	11.8022	8.49065
Maximum slope	12.80200	16.43000	11.66600
Minimum slope	7.04600	6.69400	4.83600

Unlike the simulation results with the total error model, ES obtains a higher minimum, maximum and average output fidelity compared to MQNC and QNC. All three protocols have linear correlations between the output fidelity and the accuracy of local operation, and end up with similar output fidelity as the local operation accuracy approaches to 1. While ES obtains a higher error tolerance with better qubit memories, in all three protocols, memory imperfection is the dominant error and is the main causes of faulty communication.

Chapter 7

Conclusion

Using Monte-Carlo simulation, this thesis discussed the simulated error propagation of 3 different protocols, MQNC, QNC and ES on a butterfly network.

MQNC is more sensitive to Z errors, and has no practical advantage over ES in terms of initial error tolerance. On the other hand, unlike QNC and ES, the correlation between the input and output fidelity differs from Z errors to X errors, as only X errors propagate through CZ gates. In the asymptotic limit with the artificial model of only a single error type, MQNC fares worse than either QNC and ES because both X and Z errors develop in the final 2-qubit cluster states. In general, however, the proposed protocol showed a substantial improvement of overall error tolerance compared to QNC, and is even slightly better than ES with the total error model.

Although ES still seems to be a better option with the accessibility to high performance qubit memories, one should be reminded that Buffer-Space Multiplexing requires an extra link at the bottleneck to complete the whole process in one cycle. If the network does not have extra qubits for bottleneck link, using Time-Division Multiplexing (TDM) may be another option. However, as TDM requires more waiting time compared to ES, the communication fidelity drops even more. As a conclusion, MQNC is more practical than QNC, but the choice of MQNC or ES still depends on the situation and the network topology. If resources for networking are abundant, ES may be more useful. In contrast, MQNC is more practical if resource contention is critical and needs to be resolved.

Future work

The butterfly network and the grail network are the two fundamental primitive networks with the feasibility of transmitting two symbols simultaneously from different sources to destinations via network coding [41]. This thesis does not discuss the feasibility of quantum network coding over a grail network. Furthermore, quantum circuits in general do not include any information regarding the distances between each node, and therefore has not been simulated. Simulation results for each protocol may differ significantly by taking into consideration the fact that qubits degrade while waiting for the classical feedforward operation. In the end, the simulation results that has been introduced in the thesis do not include any purification to resources. While applying purification to resources in ES is feasible, the difficulty in performing purifications to resources in MQNC and QNC is still questionable.

Acknowledgements

First and foremost, I would like to express my deepest gratitude to Associate Professor Rodney Van Meter at Keio University for his long term support through out my Bachelor's program, and allowing me to participate at different projects. The participations at the lab and at the conferences, QCNC2016 and TQC2017, became of the most valuable and irreplaceable experiences in my life.

I also acknowledge Project Research Associate Takahiko Satoh at Keio University and Doctor Shota Nagayama at Eötvös Loránd University for being always a supportive supervisor. I gained much of the important knowledge by sitting next to and learning from them. Without their gentle guidance, I would have never enjoyed researching and have never decided to proceed to the Master's program.

I would also like to thank other members in the AQUA lab, Takafumi Oka for his passion and willingness to discuss and talk about any topic, which I really enjoyed. Shinnosuke Ozawa for his great effort in ORF that also motivated me, Shin Nishio and Daikoku Neil Hideo for their eager participation at the lab, which encouraged me to work even more.

I thank Keiko Shigeta for her kindness. She was always supportive, and I enjoyed working with her in all kinds of things.

I also thank Peter Tien for frequently bringing a lot of food in my house and staying up late doing nothing productive for the last few months. I liked it.

Finally, I am grateful to all members in Tokuda, Murai, Kusumoto, Nakamura, Takashio, Uehara, Van Meter, Mitsugi, Nakazawa and Takeda Laboratories for all the supports.

Bibliography

- [1] R. Ahlswede, Ning Cai, S. Y.R. Li, and R. W. Yeung. Network information flow. *IEEE Trans. Inf. Theor.*, 46(4):1204–1216, September 2006.
- [2] Mandar Chitre and Wee-Seng Soh. Network coding to combat packet loss in underwater networks. In *Proceedings of the Fifth ACM International Workshop on UnderWater Networks*, WUWNet ’10, pages 5:1–5:6, New York, NY, USA, 2010. ACM.
- [3] Samih Abdul-Nabi, Ayman Khalil, Philippe Mary, and Jean-François Hélard. Efficient network coding solutions for limiting the effect of packet loss. *EURASIP J. Wireless Comm. and Networking*, 2017:35, 2017.
- [4] Takahiko Satoh, François Le Gall, and Hiroshi Imai. Quantum network coding for quantum repeaters. *Phys. Rev. A*, 86:032331, Sep 2012.
- [5] Richard Feynman and Peter W. Shor. Simulating physics with computers. *SIAM journal on Computing*, Vol. 26, pp. 1484–1509, 1982.
- [6] D. Deutsch. Quantum theory, the church-turing principle and the universal quantum computer. *Proceedings of the Royal Society of London A: Mathematical, Physical and Engineering Sciences*, 400(1818):97–117, 1985.
- [7] C. H. Bennett and G. Brassard. Quantum cryptography: Public key distribution and coin tossing. *Proceedings of IEEE International Conference on Computers, Systems, and Signal Processing*, Vol. 11, pp. 175–179, 1984.
- [8] C. H. Bennett and G. Brassard. The dawn of a new era for quantum cryptography: The experimental prototype is working! *Sigact News*, Vol. 20, no. 4, pp. 78–82, 1989.
- [9] Peter W. Shor. Algorithms for quantum computation: discrete logarithms and factoring. *Proceedings 35th Annual Symposium on Foundations of Computer Science*, Vol. 35, pp. 124134, 1994.
- [10] Charles H. Bennett, Gilles Brassard, Claude Crépeau, Richard Jozsa, Asher Peres, and William K. Wootters. Teleporting an unknown quantum state via dual classical and einstein-podolsky-rosen channels. *Phys. Rev. Lett.*, 70:1895–1899, Mar 1993.

- [11] Dik Bouwmeester, Jian-Wei Pan, Klaus Mattle, Manfred Eibl, Harald Weinfurter, and Zeilinger Anton. Experimental quantum teleportation. *Philosophical Transactions of the Royal Society of London A: Mathematical, Physical and Engineering Sciences*, 356(1743):1733–1737, 1998.
- [12] A. Furusawa, J. L. Sørensen, S. L. Braunstein, C. A. Fuchs, H. J. Kimble, and E. S. Polzik. Unconditional quantum teleportation. *Science*, 282(5389):706–709, 1998.
- [13] H.-J. Briegel, W. Dür, J. I. Cirac, and P. Zoller. Quantum repeaters: The role of imperfect local operations in quantum communication. *Phys. Rev. Lett.*, 81:5932–5935, Dec 1998.
- [14] W. Dür, H.-J. Briegel, J. I. Cirac, and P. Zoller. Quantum repeaters based on entanglement purification. *Phys. Rev. A*, 59:169–181, Jan 1999.
- [15] Richard Jozsa. Fidelity for mixed quantum states. *Journal of Modern Optics*, vol. 41, Issue 12, p.2315-2323, 1994.
- [16] M. A. Horne M. Zukowski, A. Zeilinger and A. K. Ekert. Event-ready-detectors bell experiment via entanglement swapping. *Phys. Rev. Lett.* 71, 4298, 1993.
- [17] Daniel E. Browne Robert Raussendorf and Hans.J. Briegel. Measurement-based quantum computation with cluster states. *Phys. Rev. A*, Vol. 68, 2003.
- [18] Xinlan Zhou, Debbie W. Leung, and Isaac L. Chuang. Methodology for quantum logic gate constructions. *Phys. Rev. A*, 62,052316, 2000.
- [19] Juan Yin, Yuan Cao, Yu-Huai Li, Sheng-Kai Liao, Liang Zhang, Ji-Gang Ren, Wen-Qi Cai, Wei-Yue Liu, Bo Li, Hui Dai, Guang-Bing Li, Qi-Ming Lu, Yun-Hong Gong, Yu Xu, Shuang-Lin Li, Feng-Zhi Li, Ya-Yun Yin, Zi-Qing Jiang, Ming Li, Jian-Jun Jia, Ge Ren, Dong He, Yi-Lin Zhou, Xiao-Xiang Zhang, Na Wang, Xiang Chang, Zhen-Cai Zhu, Nai-Le Liu, Yu-Ao Chen, Chao-Yang Lu, Rong Shu, Cheng-Zhi Peng, Jian-Yu Wang, and Jian-Wei Pan. Satellite-based entanglement distribution over 1200 kilometers. *Science*, Vol.356, Issue 6343, pp. 1140-114, 2017.
- [20] Hou Shun Poh, Siddarth K. Joshi, Alessandro Cerè, Adán Cabello, and Christian Kurtsiefer. Approaching tsirelson’s bound in a photon pair experiment. *Phys. Rev. Lett.*, 115:180408, Oct 2015.
- [21] B. Hensen, H. Bernien, A. E. Dréau, A. Reiserer, N. Kalb, M. S. Blok, J. Ruitenberg, R. F. L. Vermeulen, R. N. Schouten, C. Abellán, W. Amaya, V. Pruneri, M. W. Mitchell, M. Markham, D. J. Twitchen, D. Elkouss, S. Wehner, T. H. Taminiau, and R. Hanson. Loophole-free bell inequality violation using electron spins separated by 1.3 kilometres. *Nature*, 526:682–686, 2015.
- [22] N. Brunner, D. Cavalcanti, S. Pironio, V. Scarani, and S. Wehner. Bell nonlocality. *Reviews of Modern Physics*, 86:419–478, April 2014.

- [23] Anupam Garg and N. D. Mermin. Detector inefficiencies in the einstein-podolsky-rosen experiment. *Phys. Rev. D*, 35:3831–3835, Jun 1987.
- [24] Philippe H. Eberhard. Background level and counter efficiencies required for a loophole-free einstein-podolsky-rosen experiment. *Phys. Rev. A*, 47:R747–R750, Feb 1993.
- [25] J. Barrett, D. Collins, L. Hardy, A. Kent, and S. Popescu. Quantum nonlocality, Bell inequalities, and the memory loophole. *Phys. Rev. A*, 66(4):042111, oct 2002.
- [26] B. P. Lanyon, P. Jurcevic, M. Zwerger, C. Hempel, E. A. Martinez, W. Dür, H. J. Briegel, R. Blatt, and C. F. Roos. Measurement-based quantum computation with trapped ions. *Phys. Rev. Lett.*, 111:210501, Nov 2013.
- [27] Shota Yokoyama, Ryuji Ukai, Seiji C. Armstrong, Chanond Sornphiphatphong, Toshiyuki Kaji, Shigenari Suzuki, Junichi Yoshikawa, Hidehiro Yonezawa, Nicolas C. Menicucci, and Akira Furusawa. Ultra-large-scale continuous-variable cluster states multiplexed in the time domain. *Nature Photonics* 7, 982986, 2013.
- [28] I. Schwartz, D. Cogan, E. R. Schmidgall, Y. Don, L. Gantz, O. Kenneth, N. H. Lindner, and D. Gershoni. Deterministic generation of a cluster state of entangled photons. *Science*, 2016.
- [29] N. H. Lindner and T. Rudolph. Proposal for pulsed on-demand sources of photonic cluster state strings. *Physical Review Letters* 103, 113602, 2009.
- [30] Masahito Hayashi. Prior entanglement between senders enables perfect quantum network coding with modification. *Phys. Rev. A*, Vol. 76, p.040301, 2007.
- [31] Debbie Leung, Jonathan Oppenheim, and Andreas Winter. Quantum network communication the butterfly and beyond. *IEEE Transactions on Information Theory*, Vol. 56, pp. 34783490, 2007.
- [32] Hirotada Kobayashi, François Gall, Harumichi Nishimura, and Martin Rötteler. General scheme for perfect quantum network coding with free classical communication. In *Proceedings of the 36th International Colloquium on Automata, Languages and Programming: Part I*, ICALP '09, pages 622–633, Berlin, Heidelberg, 2009. Springer-Verlag.
- [33] Hirotada Kobayashi, Franois Le Gall, Harumichi Nishimura, and Martin Rötteler. Perfect quantum network communication protocol based on classical network coding. *2010 IEEE International Symposium on Information Theory*, pages 2686–2690, 2010.
- [34] Hirotada Kobayashi, Franois Le Gall, Harumichi Nishimura, and Martin Rötteler. Constructing quantum network coding schemes from classical nonlinear protocols. *2011 IEEE International Symposium on Information Theory Proceedings*, pages 109–113, 2011.

- [35] Masahito Hayashi, Kazuo Iwama, Harumichi Nishimura, Rudy Raymond, and Shigeru Yamashita. Quantum network coding. *Symposium on Theoretical Aspects of Computer Science*, pp. 610-621, 2007.
- [36] Michael Epping, Hermann Kampermann, and Dagmar Bruß. Quantum router with network coding. *New Journal of Physics*, Vol. 18, 2016.
- [37] Cody Jones, Danny Kim, Matthew T. Rakher, Paul G. Kwiat, and Thaddeus D. Ladd. Design and analysis of communication protocols for quantum repeater networks. *New Journal of Physics*, Volume 18, 2016.
- [38] Sreraman Muralidharan, Linshu Li, Jungsang Kim, Norbert Lütkenhaus, Mikhail D. Lukin, and Liang Jiang. Optimal architectures for long distance quantum communication. *Scientific Reports 6, Article number: 20463*, 2016.
- [39] Shota Nagayama. Distributed quantum computing utilizing multiple codes on imperfect hardware. *PhD thesis, Keio University*, 2016.
- [40] W. Dür, H.-J. Briegel, J. I. Cirac, and P. Zoller. Quantum repeaters based on entanglement purification. *Phys. Rev. A 59:169, 1999*, 1998.
- [41] Chih-Chun Wang and Ness B. Shroff. Beyond the butterfly – a graph-theoretic characterization of the feasibility of network coding with two simple unicast sessions. *IEEE International Symposium on Information Theory*, 2007.